THE EFFECTS OF ATMOSPHERIC HEAT TREATMENTS ON TiO_2 NANOTUBE

ANODES FOR LITHIUM-ION BATTERIES

by

Andreas Savva

A thesis

submitted in partial fulfillment

of the requirements for the degree of

Master of Science in Materials Science and Engineering

Boise State University

August 2018

BOISE STATE UNIVERSITY GRADUATE COLLEGE

DEFENSE COMMITTEE AND FINAL READING APPROVALS

of the thesis submitted by

Andreas Savva

Thesis Title: The Effects of Atmospheric Heat Treatments on TiO_2 Nanotube Anodes for Lithium-Ion Batteries

Date of Final Oral Examination: 17 April 2018

The following individuals read and discussed the thesis submitted by student Andreas Savva, and they evaluated his presentation and response to questions during the final oral examination. They found that the student passed the final oral examination.

Hui (Claire) Xiong, Ph.D.	Chair, Supervisory Committee
Rick Ubic, Ph.D.	Member, Supervisory Committee
Dmitri Tenne, Ph.D.	Member, Supervisory Committee

The final reading approval of the thesis was granted by Hui (Claire) Xiong, Ph.D., Chair of the Supervisory Committee. The thesis was approved by the Graduate College.

ACKNOWLEDGEMENTS

ABSTRACT

The effects of various heat treatments on the physical and electrochemical properties of anatase TiO_2 nanotubes were studied in this work. Well-ordered TiO_2 nanotubes were grown via electrochemical anodization and annealed at 450°C to induce a phase transformation to anatase. The heat treatments were conducted under atmospheres of O_2, Ar, N_2, and water vapor (WV) to create different point defects. The oxygen-deficient atmospheres were used to generate oxygen vacancies in the TiO_2 nanotubes, while the water vapor treatment was used to create Ti vacancies by stabilizing them via the protonation of O sites. Computational models of anatase TiO_2 with oxygen or titanium vacancies were created to predict the effect of the defects on the band structure and electrical properties. Two-point conductivity measurements and Mott-Schottky characterizations were conducted to evaluate the electrical conductivity and charge carrier concentration of TiO_2 nanotube samples and compared to the predicted effects of the heat treatments. Scanning electron microscopy and x-ray diffraction were used to study the nanostructure morphology. Additional characterization techniques such as Raman spectroscopy were used to study the generation of the respective point defects. The anatase nanotubes synthesized under different atmospheres were then used as anodes in lithium-ion batteries. The N_2- and WV-treated samples exhibited the largest increase in capacity, while the Ar-treated sample had a slight capacity increase compared to the stoichiometric O_2-treated control sample. Further electrochemical testing revealed that the WV-treated sample had the highest Li diffusivity.

TABLE OF CONTENTS

LIST OF TABLES

LIST OF ABBREVIATIONS

CCD	Charge Coupled Device
DFT	Density Functional Theory
DI	Deionized
EIS	Electrochemical Impedance Spectroscopy
FWHM	Full Width at Half Maximum
GGA	Generalized Gradient Approximation
LIB	Lithium-Ion Battery
PBE	Perdew-Burke-Ernzerhof
SEI	Solid Electrolyte Interphase
SEM	Scanning Electron Microscope
VASP	Vienna Ab-Initio Simulation Package
WV	Water Vapor
XRD	X-Ray Diffraction

CHAPTER ONE: INTRODUCTION

1.1 Overview

Greenhouse gas emission from the consumption of fossil fuels is one of the most significant issues facing the planet today. These emissions, particularly carbon dioxide, have increased dramatically since the middle of the nineteenth century[1]. The increase in greenhouse gases present in Earth's atmosphere has correlated with an increase in global temperatures by almost 1°C [2]. The consequences of global warming are dire, as a continued increase in temperature will result in more extreme weather patterns, ocean acidification, and sea level rise[2-3]. To prevent these events from occurring, the excessive generation of carbon dioxide and other greenhouse gases must be mitigated.

The largest contributor to anthropogenic greenhouse gas emissions has been the energy sector[3]. This component accounts for the fuels that are burned to power neighborhoods and businesses and for the emissions produced by various forms of transportation; therefore new energy sources that are sustainable and non-polluting must be found to reduce greenhouse gas emissions[3]. Wind and solar energy are capable of resolving these issues for grid application but are plagued by inherent intermittency[4-6]. Transportation requires an alternative "fuel" that allows for similar performance to internal combustion engines without generating emissions. Both of these problems can be addressed by energy storage technology.

Grid storage solutions need to be dynamic and resilient, as they must be capable of discharging large amounts of energy very quickly. Furthermore, they must be able to last for many years in order to be cost-effective[7]. In transportation, energy storage technology must be extremely energy dense, while maintaining a high degree of safety[8]. Flywheels and pumped storage systems are possible grid energy storage solutions, while fuel cells and supercapacitors have been explored as options for the transportation industry. On the other hand, batteries are capable of being implemented in both sectors as they are flexible enough to address the required demands[9]. Lithium-ion batteries (LIBs) are particularly useful, as they have high specific capacity and good rate capability, which allows them to be used across a broad spectrum of performance requirements[10-12].

1.2 Lithium-Ion Batteries

LIBs are secondary batteries, which means they are capable of being charged repeatedly. The foundation of their rechargeability is based on the shuttling of lithium ions. During battery operation, lithium ions are shuttled back and forth between the anode and cathode; the ions will travel to the anode when the battery is charging and to the cathode when the battery is providing electricity[13-15]. Upon arrival at an electrode, the lithium ions intercalate into the vacant sites in a material's structure (i.e., intercalation sites), where electrons come to meet electroneutrality[5, 14-16]. When operating at low potentials (e.g, 1 V vs. Li/Li$^+$), anode materials react with electrolytes, which might form solid electrolyte interphases (SEI) on the electrode surface. Thus, the formation of a SEI layer is crucial to the effective performance of a LIB[9]. While the consumption of the electrolyte does result in some irreversible capacity loss, the SEI layer stabilizes the

system as it prevents further electrolyte-electrode reactions. Consequently, its formation minimizes losses that could have occurred with additional cycling[9].

The inherent properties of the materials selected for a LIB are also important to the performance of the system. An ideal electrode for a LIB allows Li^+ ions to quickly diffuse in and out of the structure with little change to the electrode's volume or crystallographic integrity[5, 15]. These traits enable good rate capability and mitigate degradation due to cycling. Electrodes should also have good electronic conductivity for high rate capability[9, 17]. It is also critical that the electrolyte present in the cell conducts ions but is electronically insulating[9]. Much of the current research on LIBs focuses on improving electrode materials so that they are safer, more efficient, last longer, and have higher capacity[11, 13, 18-19].

1.3 Anode Materials

1.3.1 Graphite as an Anode

Graphite is one of the most popular anode materials in LIBs for a number of reasons. It has a high theoretical capacity of 372 mAh/g and is relatively abundant[12, 20-21]. Furthermore, it has minimal volumetric expansion when Li intercalates in between its graphene sheets[14-15]. Despite its benefits, there are some safety concerns that arise when using graphite. The lithium intercalation potential of graphite is about 0.1 V vs. Li/Li^+, which is very close to the lithium plating potential[21-23]. This means that it is very likely for lithium ions to plate on the surface of graphite rather than intercalating into the graphite host. The main consequence of lithium plating is the formation of dendrites, which can grow to pierce the separator, short-circuit the battery, and induce thermal

runaway[21-22]. As a result, different materials need to be found to overcome these problems.

1.3.2 TiO$_2$ Anode

Titanium dioxide (TiO$_2$) is a promising alternative to graphite. The three most common polymorphs of TiO$_2$ are anatase (*I4$_1$/amd*), rutile (*P4$_2$/mnm*), and brookite (*Pbca*)[22-24]. Anatase is commonly used in batteries because its crystallographic structure allows for greater amounts of intercalated Li$^+$ ions compared to other phases of TiO$_2$[24]. While it has a slightly lower theoretical capacity (335 mAh/g) compared to graphite, TiO$_2$ has a higher intercalation potential (~1.5-1.8 V), which eliminates issues about lithium plating[18, 21-25]. TiO$_2$ is also cheap, abundant, and environmentally benign[18, 21, 25]. In addition, TiO$_2$ has shown good structural stability upon cycling, as it typically expands about only 4% during lithium intercalation, compared to the 10% expansion that occurs in graphite[22, 26-27]. Despite its benefits, TiO$_2$ has not yet been developed as a commercial anode material for LIBs because of its poor conductivity and lithium ion diffusivity[20-21, 28]. These limitations must be overcome in order for TiO$_2$ to replace and surpass graphite as the premier anode material in LIBs.

1.4 Strategies for the Improvement of TiO$_2$

1.4.1 Nanostructuring

One common approach to improve the electrochemical performance of TiO$_2$ is by nanostructuring the material. Due to their reduced size, nanostructures can have superior physiochemical properties compared to bulk materials[20, 28]. Nanostructured TiO$_2$ has been shown to have a greater conductance and ion diffusivity compared to its bulk counterpart because the distances travelled by the electrons and ions are much shorter due to the

dramatic increase in specific surface area[18, 20-21, 25, 28]. Nanostructured TiO_2 can be created through a number of different experimental processes, such as anodization, sol-gel techniques, and hydrothermal methods[29-32].

1.4.2 Point Defect Generation

The generation of point defects has also been shown to improve the electrochemical properties of TiO_2. These defects can be introduced into the material through various techniques like substitutional doping and ion irradiation[33-36]. One particularly effective yet simple method used to generate point defects is atmospheric heat treatment. When TiO_2 is heated to high temperatures in different atmospheres, a number of effects can occur. Oxygen-deficient environments such as vacuum, Ar, and N_2, have been shown to create oxygen vacancies[37-40]. The hydrogenation of TiO_2 via H_2 atmospheric treatment has also been used to generate oxygen vacancies[37, 41-42]. Other environments, such as NH_3, can dope TiO_2 by introducing substitutional N atoms into the structure[36, 43].

1.5 Research Objectives

The objective of this work is to elucidate the effect that different point defects may have on the electrochemical performance of anatase TiO_2 nanotubes used as anodes in LIBs. These defects were generated by annealing the samples under various atmospheres. Oxygen-deficient atmospheres of Ar and N_2 were used to develop oxygen vacancies, while a WV atmosphere was used to create titanium vacancies. The formation of the defects was confirmed by measuring the electrical properties of the samples, as well as by other characterization techniques such as Raman spectroscopy. The annealed samples were then subjected to electrochemical measurements to determine whether the

generation of point defects improved performance. From our results, we were able to conclude that electrical conductivity cannot be the only material property considered in predicting electrode performance.

CHAPTER TWO: BACKGROUND INFORMATION

2.1 TiO$_2$ Nanotube Growth via Anodization

Anodization is a very useful technique for creating nanostructures, as it enables growth in a self-organized fashion on a conductive Ti substrate without the need for binders[29, 44-45]. To create TiO$_2$ nanotubes in this manner, a constant voltage is applied to the Ti substrate that acts as the working electrode in a two-electrode electrochemical cell; the Ti undergoes oxidation to generate Ti^{4+} ions[29]. The counter electrode is an inert metal, such as Pt, where H$_2$ is evolved due to the splitting of water to complete the redox reaction for the electrochemical cell[29]. The electrolyte must contain fluoride ions and some amount of water. The electric field generated by the applied voltage causes the water in the electrolyte to deprotonate, and the resulting O^{2-} ion migrates to the Ti electrode and reacts with Ti^{4+} to form TiO$_2$[29]. The subsequent growth of the oxide layer is due to the field-assisted transport of the Ti^{4+} and O^{2-} ions through the oxide. Fluoride ions are crucial to the development of nanotubes; if they were absent, a compact layer of TiO$_2$ would form. F$^-$ ions react with Ti^{4+} ions or TiO$_2$ to form soluble [TiF$_6$]$^{2-}$ species, which leads to the etching of the TiO$_2$ layer[29, 45]. The competition between etching and growth results in the formation of nanotubes[21, 37]. The accumulation of fluoride ions at structural boundaries (i.e., tube walls) causes tube formation as opposed to pores. In addition, plastic flow enables the tubes to grow to longer-than-expected lengths due to inherent stresses pushing up the tube walls[29]. The applied voltage and electrolyte components,

along with other parameters, can be fine-tuned to alter the tube dimensions and obtain a variety of structures[29, 44-45].

2.2 Kröger-Vink Equations for Generated Point Defects in TiO$_2$

The generation of point defects in TiO$_2$ and other metal oxides has been shown to improve performance in a number of applications. Materials used in photocatalysis, solar cells, and batteries all have demonstrated superior properties with the introduction of defects[37, 40-41, 46-50]. If TiO$_2$ is annealed under oxygen-deficient environments (e.g., in pure Ar or N$_2$), oxygen vacancies can form and generate free electrons (**Equation 2.1**) and reduce Ti (**Equation 2.2**) [37, 39, 41, 51-52].

$$TiO_2 \rightarrow 2V_O^{\cdot\cdot} + O_{2(g)} + Ti_{Ti}^x + 4e^-$$
Equation 2.1

$$TiO_2 \rightarrow 2V_O^{\cdot\cdot} + O_{2(g)} + Ti_{Ti}' + 3e^-$$
Equation 2.2
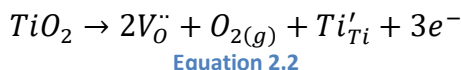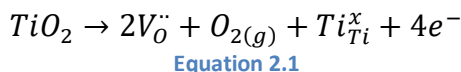
Oxygen vacancy formation may result in higher conductivity, improved rate capability, and higher capacity[37-39, 41, 49, 51]. During heat treatments where oxygen is present, any oxygen vacancies already present in the sample will be eliminated, making TiO$_2$ more stoichiometric (**Equation 2.3**).

$$O_{2(g)} + V_O^{\cdot\cdot} \rightarrow O_O^x$$
Equation 2.3
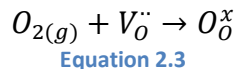
Titanium vacancies may form if water vapor (WV) is added to an oxygen-rich annealing environment. The water vapor may protonate existing oxygen sites and vacancies, which develop a positive charge, and subsequently stabilize Ti vacancies present in the sample (**Equation 2.4, Equation 2.5**). It has been shown in TiO$_2$ and other metal oxides that cation vacancies may provide more sites for lithium intercalation and therefore increase capacity[35, 47, 53-55].

$$V_{Ti}^{''''} + 2V_{\ddot{O}} + O_2 + 2H_2O \rightarrow V_{Ti}^{''''} + 4OH_{\dot{O}}$$
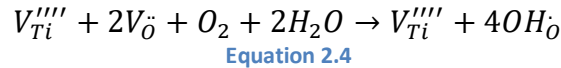
<div align="center">Equation 2.4</div>

The protonated oxygen sites that stabilize the Ti vacancies may also enhance the charge-storage ability and capacitance of the system[56-57]. During Li$^+$ intercalation, the lithium ions can exchange with protons without affecting the charge balance, which would provide additional sites to store Li$^+$ and thus also increase capacity (***Equation 2.5***) [54].

$$(OH)_{\dot{O}} + Li^+ \rightarrow (OLi)_{\dot{O}} + H^+$$
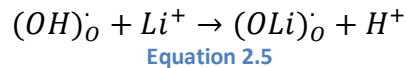
<div align="center">Equation 2.5</div>

2.3 Mott-Schottky Analysis

Mott-Schottky analysis is an electrochemical impedance technique that is used to measure the charge carrier density of a semiconductor. When performing Mott-Schottky tests, it is imperative that the appropriate frequency is selected for analysis. The charge carrier density of the sample is determined from space-charge capacitance (C_{sc}), which is obtained from Z'', the imaginary contribution to impedance, and the frequency, f (***Equation 2.6***)[58-59].

$$C_{sc} = -\frac{1}{2\pi f Z''}$$

<div align="center">Equation 2.6</div>

If the frequency is too low, surface-state capacitance (C_{ss}) will contribute to the total capacitance, incorrectly skewing results towards higher carrier density values[58]. In addition, the real contribution to impedance, Z', would also vary with frequency[58]. The following equation (***Equation 2.7***) relates the charge carrier density to the capacitance of the sample, where q is the charge of an electron, ε is the dielectric constant (assumed to be a constant value of 31 for anatase[60]), ε_0 is the vacuum permittivity constant, N_D is the charge carrier density, A is the geometric surface area, V_{fb} is the flat-band potential, V is

the applied potential, k is Boltzmann's constant, and T is the absolute temperature[42, 52, 59-60].

$$C_{sc}^{-2} = \left(\frac{2}{q\epsilon\epsilon_0 N_D A^2}\right)\left(V - V_{fb} - \frac{kT}{q}\right)$$

Equation 2.7 is then differentiated with respect to the voltage and manipulated to the below form (*Equation 2.8*) where the slope of the plot's linear region $\frac{dC^{-2}}{dV}$ is used to obtain the charge carrier density.

$$N_D = \frac{2}{q\epsilon\epsilon_0 A^2}\left(\frac{dC^{-2}}{dV}\right)^{-1}$$

TiO_2 is an n-type semiconductor and each Mott-Schottky curve has a positively sloped linear region[52, 59, 61-63]. According to *Equation 2.8*, as the slope becomes less steep, the charge carrier (electron) density increases.

2.4 Introduction to Electrochemical Impedance Spectroscopy (EIS)

EIS is an electrochemical technique that is used to understand processes occurring at different time scales. Nyquist plots are generally used in EIS analysis and relate the real contribution to impedance, Z', to Z'', the imaginary contribution to impedance[64-66]. These plots are then used to obtain values such as the charge-transfer resistance and Li diffusivity of an electrode[64, 66]. Nyquist plots of an electrode can be divided into three major regions, which correspond to the areas subjected to analysis during EIS. Electrolyte and surface film phenomena and properties correspond to the first semicircle in the high frequency region of the plot[64, 66]. The high-to-medium frequency region follows and corresponds to the charge-transfer process at the electrode-electrolyte interface, which is

also represented by another semicircle component[64, 66]. The low frequency region is used to describe phenomena in the bulk electrode, and is represented by the linear tail of the plot[64, 66].
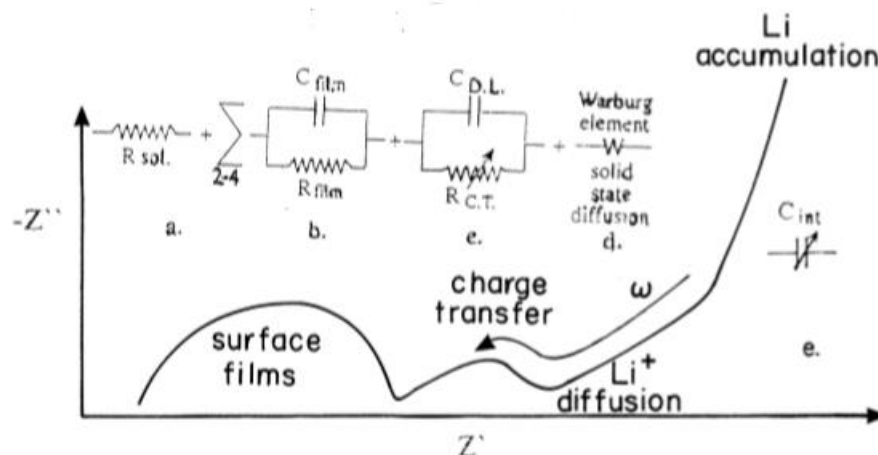
Figure 2.1   Representative Nyquist plot obtained from EIS measurements[66]

To obtain information of the different processes (e.g., charge-transfer resistance, Li diffusivity, etc.), an equivalent circuit model must be constructed and fitted to the experimentally measured data[64-65]. The circuit is comprised of components like resistors and capacitors which are representative of the phenomena occurring during the electrochemical process. Warburg elements are of particular interest in an equivalent circuit, as they describe Li diffusion in the bulk of the sample[64-66]. Great care must be taken when developing the circuit, as a variety of circuits can fit a set of experimental data very well. The equivalent circuit must be relevant to the actual experiment, otherwise any calculated values may be inaccurate.
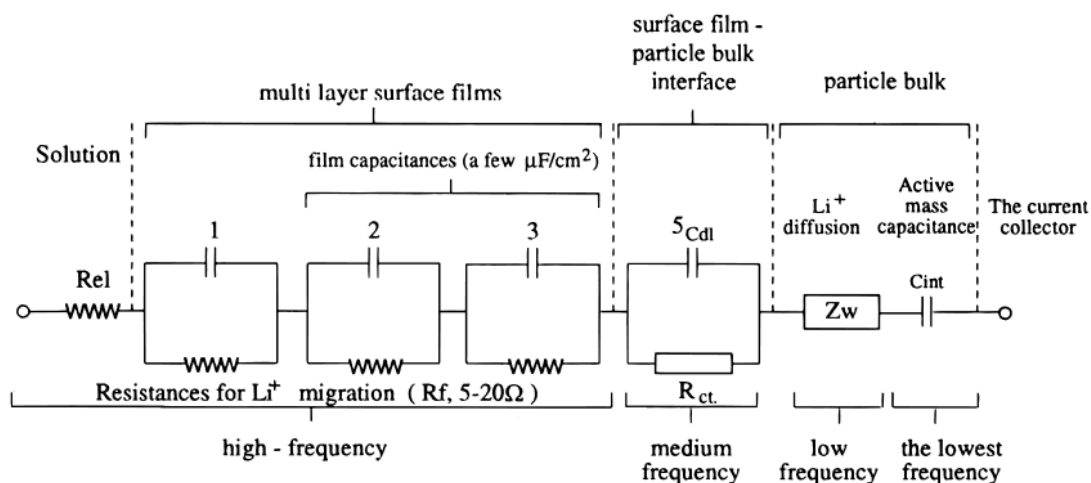
Figure 2.2   Equivalent circuit developed to fit data obtained from EIS measurements[64]

Once the most appropriate equivalent circuit is selected and fitted to the experimental data, the calculated Warburg factor σ (obtained from the Warburg element) can be used to determine the Li diffusion coefficient using ***Equation 2.9***, where R is the gas constant, T is the absolute temperature, C_{Li} is the Li concentration in the electrolyte, n is the transferred charge, F is Faraday's constant, and A is the geometric surface area[67-69].

$$D_{Li} = \frac{R^2 T^2}{2C_{Li}^2 \sigma^2 n^2 F^4 A^2}$$

Equation 2.5

2.5 Two-Point Conductivity Measurements

When nanotubes are used in batteries, electron transport occurs in one dimension along the length of the tubes. As a consequence, the conductivity perpendicular to the substrate must be effectively measured. Therefore, a two-point measurement is required to obtain the out-of-plane conductivities. It is critical to note that this value is not determined from the sheet resistance that would be measured via a traditional four-point technique, but rather the resistance across the length of the tubes[70].

Due to the different geometry in the two-point conductivity setup, the
conductivity calculation must be adjusted accordingly. The measured resistance can be
converted to resistivity using **Equation 2.10** and **Equation 2.11**, where l is the length of
the tube, r is the approximate radius of the contact, and F is the effective factor of the
nanotubes[70].

$$R = \rho * \frac{l}{s}$$

Equation 2.6

$$s = \pi r^2 * F$$

Equation 2.7

The effective factor can be determined by subtracting the porosity from 1. The porosity,
P, is calculated using the tube wall thickness, w, and the tube diameter, D (**Equation
2.12**)[70].

$$P = 1 - \frac{2\pi * w * (w + D)}{\left(\sqrt{3} * (D + 2w)^2\right)}$$

Equation 2.8

For simplification, it is assumed that the nanotubes are perfectly ordered in a
hexagonal pattern[70]. The subsequently calculated conductivity values are therefore
obtained by assuming that the tube packing is uniform within the cylinder bounded by the
contacts. It must be noted that the conductivity values are not quite accurate in spite of
the reasonable approximations. This is due to the fact that the wall thickness is likely not
uniform along the length of the tubes. Furthermore, there could be cracks along the tubes
into which the contact material could seep, which would enlarge the contact area[70].
Evidence of these factors are seen in literature, as there is a large variation in reported

two-point conductivities of TiO_2 nanotubes[38, 70-72]. Regardless of these shortcomings, this

technique can be used to detail the general trends in sample conductivity.

CHAPTER THREE: EXPERIMENTAL METHODS

3.1 Computational Modeling

To capture the electronic structure and properties of the anatase TiO_2, density functional theory (DFT) was performed using Vienna ab initio simulation package (VASP)[73]. The exchange correlation energies were described using the Perdew-Burke-Ernzerhof (PBE) pseudopotentials and generalized gradient approximation (GGA)[74]. A cut-off energy of 380 eV was chosen to account for the plane waves. To incorporate a rich electronic structure, the unit cell of the anatase phase was expanded into a 3 x 3 x 1 supercell with a Γ-centered 5 x 5 x 7 k-point mesh sampling in the Brillouin zone. The electronic structures and properties of pristine, oxygen-deficient, and Ti-deficient anatase TiO_2 were calculated from their respective ground state structures with residual forces of 0.1 eV/Å and an electronic convergence of 1×10^{-6}. The band structures of these systems were determined from this procedure. To account for the strongly correlated d orbital effect on titanium, the DFT + U scheme was applied with an on-site Coulomb potential of 8.0 eV, and the partial charge densities were also generated 2 eV above and below the Fermi energy to further study how the electron density distribution was affected by various defects[75].

3.2 Anodization of Ti Foil

Ti foil (Alfa Aesar, 32 μm thick) was cut into 4 x 4.5 cm pieces and sonicated in acetone, isopropanol, and DI water for 5 minutes each. The foil was then air-dried and

had its back protected with acrylic sheeting and packing tape (*Figure 3.1*). The back of

the foil was taped so that only one surface would form TiO_2 nanotubes. The top edge of

the foil was left exposed to maintain good electrical contact with the clips used to connect

it to the power supply. The taped foil was put into the electrochemical cell with the

exposed surface facing the Pt mesh (*Figure 3.2*). Care was taken to make sure that the

clips to which the Ti foil and Pt mesh were attached were not in solution. Otherwise, the

clips would corrode and the tube morphology could be affected. The prepared foil was

then anodized in a solution of 0.27 M NH_4F in formamide, with Pt mesh as the counter

electrode, for 30 minutes at 15 V and 0.2 A. A Teflon beaker was used for the

anodization, so that it would not be etched by the fluoride ions in solution. After

anodization was complete, the foil was dipped in DI water to remove excess solution and

then sonicated in isopropanol and DI water for three 1-second bursts each. The foil then

had its edges trimmed and backing carefully peeled off and was put to dry for several

hours in a vacuum oven at approximately 70°C.

Packing Tape

Ti Foil

Acrylic Backing
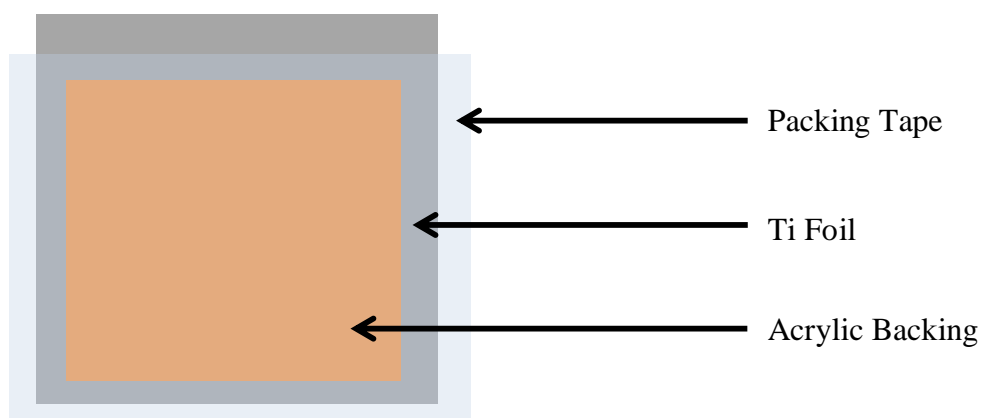
**Figure 3.1   Back of Ti foil used for anodization to grow TiO_2
nanotubes**
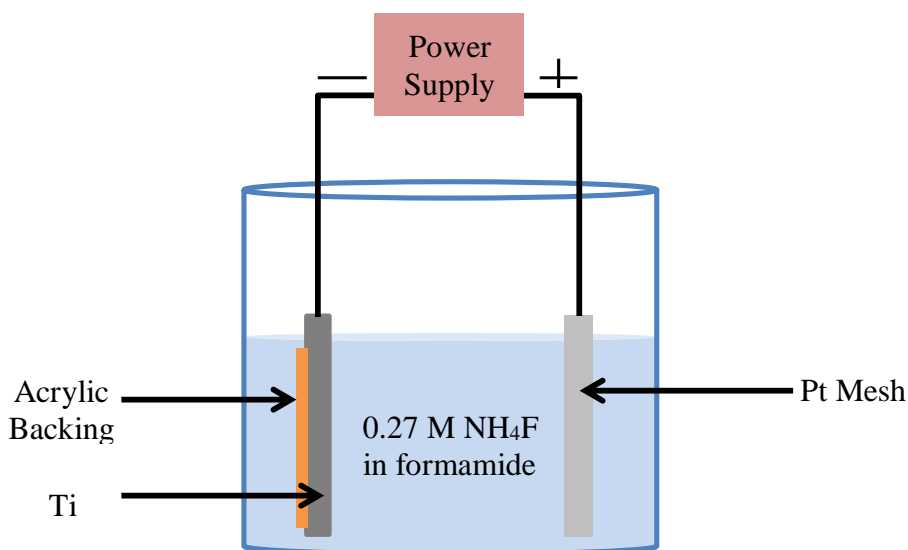
Figure 3.2   **Setup for anodization of Ti foil**

3.3 Annealing of TiO$_2$ Nanotubes

Four 15 mm discs were punched out of each anodized sample using an MTI Precision Disk Cutter. Each sample was weighed and one disc from each sample was sacrificed for active weight measurements by using scotch tape to strip the nanotubes from the Ti substrate and reweighed. The mass difference was then used to calculate the active weight of the sample, which was used to calculate its specific capacity. The other three discs were annealed in an MTI OTF-200X tube furnace under O$_2$ (80% Ar, 20% O$_2$), Ar (99.9%), N$_2$ (99.9%), or WV. The WV atmosphere was generated by bubbling O$_2$ (80% Ar, 20% O$_2$) through a DI water bath heated to 80°C (*Figure 3.3*). The samples were heated to 450°C at a rate of 1°C/min and held at 450°C for 4 hours before cooling to room temperature at a rate of 1°C/min. Before each sample was annealed, the tube furnace was pumped down to a vacuum pressure of 0.05 MPa and then purged with the target atmosphere for 5 minutes. This process was repeated 3 times and then followed by a final 30-minute purge.

The thinness of the Ti substrate made the sample prone to warping as a result of the heat treatment. To mitigate this effect, the samples were sandwiched between two glass slides with a 1 mm spacer (***Figure 3.4***). The sleeves allowed for enough gas to flow over the sample while preventing significant distortion.
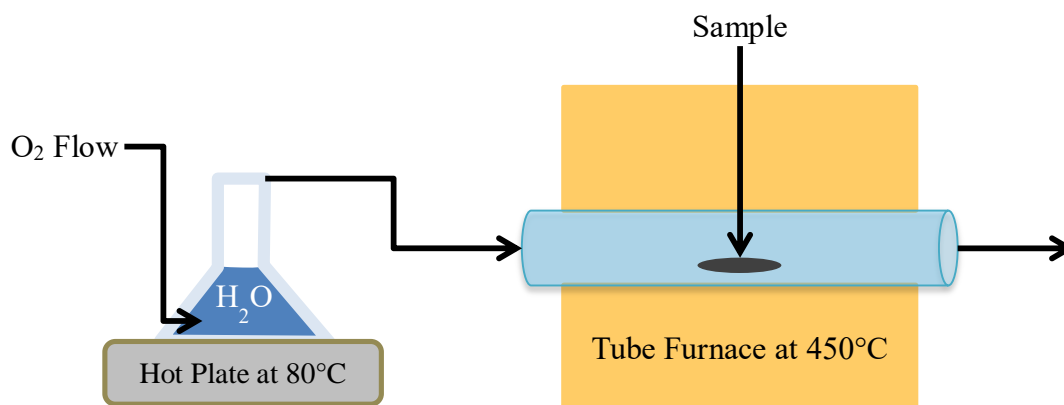
Figure 3.3   **Setup of WV heat treatment on TiO$_2$ nanotube sample**

Figure 3.4   **Cross-section of glass sleeve used to prevent sample warping during heat treatment**

3.4 Coin Cell Construction and Cycling

Coin cells were assembled in an Ar-filled glovebox (Mbraun) with an O$_2$ concentration less than 0.5 ppm. The cells used were size 2032, meaning that the cell diameter was 20 mm and the cell thickness was 3.2 mm. Each cell was constructed from bottom to top as shown in ***Figure 3***. An annealed TiO$_2$ disc was used as the working electrode and Li metal (FMC Lithium) was used as the counter electrode with two 2325 type polymer discs as the separator (Celgard) in each cell. The electrolyte was 1.2 M

LiPF$_6$ (Tomiyama) in ethylene carbonate/ethyl methyl carbonate (3:7 weight ratio). A

few drops of electrolyte were added using a micropipette to the TiO$_2$ surface and

separators before the Li metal was added during construction. A plastic gasket and spring

were added to ensure a complete and even seal upon crimping. The cells were then cycled

for 30 cycles from 0.9 to 2.5 V vs. Li/Li$^+$ at a theoretical C rate of C/20 (16.75 mA/g)

using an automated Arbin battery tester. For the rate study, the cells were tested under the

same voltage window at theoretical C rates of C/20, C/10, C/5, C/2, 1C, and 5C for 5

cycles each. The cells underwent cycling in a ThermoFisher Heratherm incubator at a

constant temperature of 25°C.

Top Casing

Spring

Current Collector

Lithium metal

Separator

TiO$_2$ NT Anode

Current Collector

Plastic Gasket

Bottom Casing
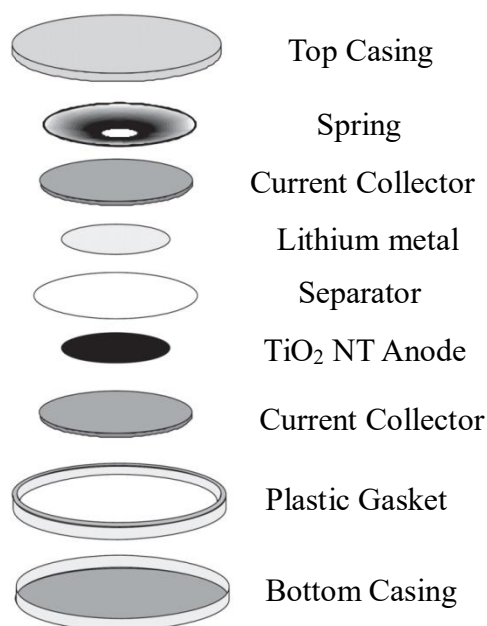
Figure 3.5   **Construction of coin cell used for electrochemical characterizations[76]**

3.5 Mott-Schottky Characterization Setup

For Mott-Schottky analysis, 2 x 2 cm samples of annealed TiO$_2$ nanotubes were

masked on both sides with Kapton tape, with a 15 mm diameter area left exposed on one

side. To prevent any extraneous contribution from the setup, the clip to which the sample was attached was also covered with Kapton tape. A Pt mesh was used as the counter electrode in an aqueous 1 M KOH solution. A Ag/AgCl reference electrode was used. Mott-Schottky analysis was subsequently performed with the aforementioned setup using the SPEIS program on a Bio-Logic VMP-300. Samples were analyzed in a frequency range from 100 kHz to 100 mHz with an excitation voltage of 10 mV from 0.1 to -1 V vs. Ag/AgCl in 0.05 V increments. There was a wait period of 30 seconds before each potential step and 5 data points were reported per decade. In addition, the program was set to wait 1 period before each frequency and 5 recorded values were averaged before data was outputted. The allowable voltage range was set to -2.5 to 2.5 V with no drift correction. The current range was put to the Auto setting and the bandwidth was set to 8.

Clip

Ti Foil with annealed TiO_2

Kapton Tape
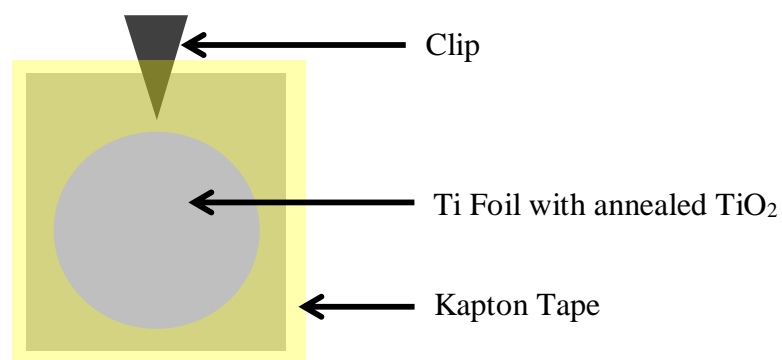
Figure 3.6   Front of TiO_2 nanotube sample used for Mott-Schottky characterization
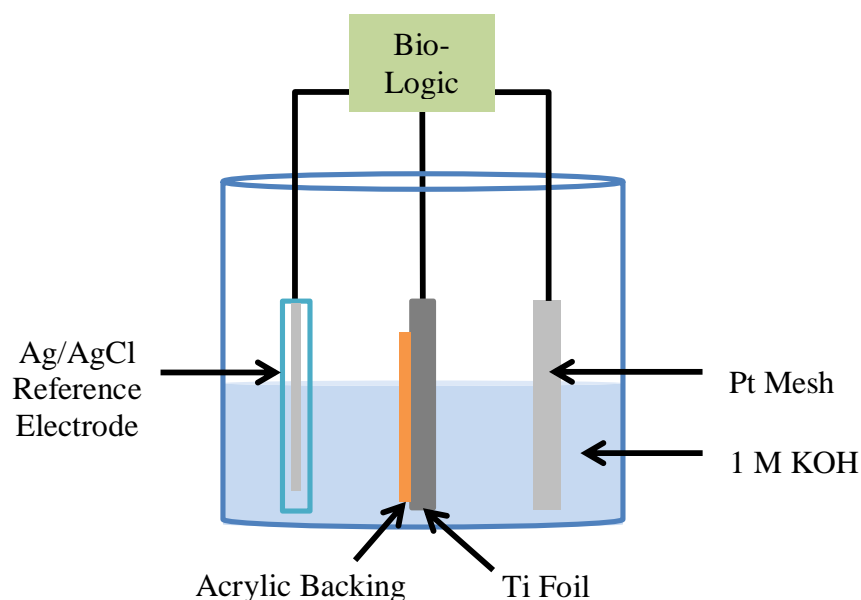
Figure 3.7 **Setup for Mott-Schottky characterization of heat treated anatase TiO$_2$ nanotubes**

3.6 Two-Point Conductivity Setup

Two-point conductivity measurements were used to determine the out-of-plane conductivity of the nanotubes. A silver paint contact was placed on the nanotube surface with another on the back of the Ti foil; copper wire was attached to the bottom to serve as a contact point for the instrument (*Figure 3.8*). The contacts were about 2 mm in diameter. Two probes were put on each contact, where one was used to apply a current of 10 μA and the other used to measure voltage. A Keithley 237 High Voltage Source Measure Kit was used to apply the current to each sample and a Keithley 2000 Multimeter was used to record the resulting voltage. The applied bias was then reversed to ensure the validity of the measured value.
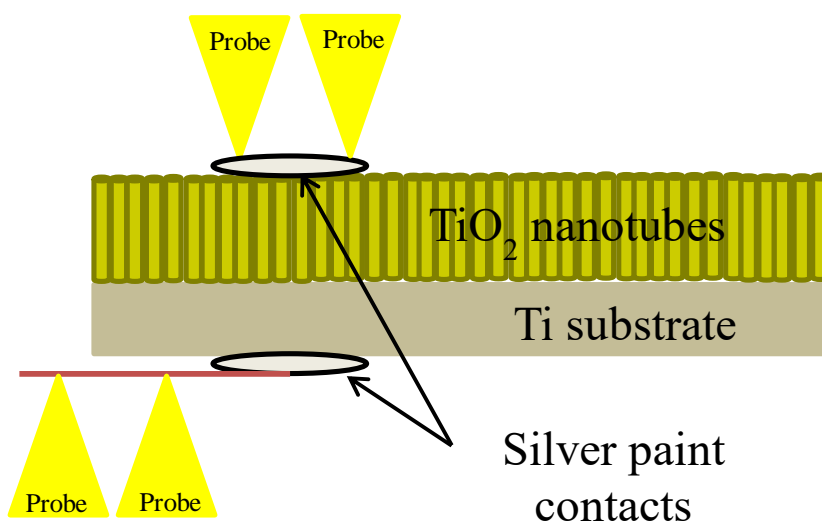
Figure 3.8   **Setup of two-point conductivity measurement of anatase TiO₂ nanotubes on a Ti substrate**

3.7 XRD

XRD was performed using a Rigaku MiniFlex 600 with a 600 W generator and Cu target; 2θ was varied from 20-85°. A LaB_6 standard was used to account for the instrumental broadening of the machine. To determine whether strain was present in the nanotubes as a consequence of annealing under the different atmospheres, Williamson-Hall plots were created using ***Equation 3.1***, where B is the FWHM of the peak, θ is the measurement angle, ε is the strain, K is the shape factor, and L is the crystallite size[77]. The shape factor was assumed to be 0.9[78-79]. From this equation, it is apparent that ε can be determined from the slope of the line, while the crystallite size can be obtained from the y-intercept.

$$B \cos \theta = 4\epsilon \sin \theta + \frac{K\lambda}{L}$$

Equation 3.1

The Scherrer equation (***Equation 3.2***) was used to calculate the crystallite size present in the annealed nanotubes, where L is the crystallite size, K is the shape factor, λ is the x-ray wavelength, B is the FWHM of the peak, and θ is the measurement angle[80].

$$L = \frac{K\lambda}{B \cos \theta}$$

Equation 3.2

3.8 EIS

EIS was done using the PEIS program on a Bio-Logic VMP-300 using a three-electrode EL cell. Samples were analyzed in a frequency range from 100 kHz to 5 mHz with an excitation voltage of 5 mV. 5 data points were reported per decade. In addition, the program was set to wait 0.1 periods before each frequency and 5 recorded values were averaged before data was outputted. The allowable voltage range was set to 0 to 5 V with no drift correction. The current range was put to the Auto setting and the bandwidth was set to 8. The voltage was set as the open-circuit potential for each sample and Li metal was used for the counter and reference electrode. The electrolyte was 1.2 M LiPF$_6$ (Tomiyama) in ethylene carbonate/ethyl methyl carbonate (3:7 weight ratio) along with a glassy fiber separator. The experimental data was then fit using the Zfit function via EC-Lab software. The equivalent circuit used to fit the data and obtain the Warburg factor is shown in ***Figure 3.9***.
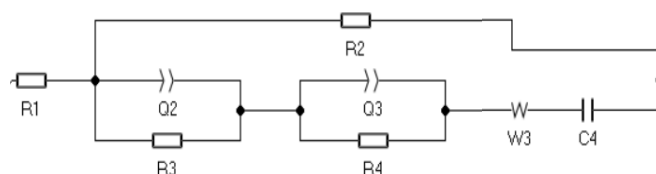
Figure 3.9: Equivalent circuit used to fit EIS data for anatase TiO$_2$ nanotubes annealed in different atmospheres

In the equivalent circuit, R1 represents the electrolyte resistance. The components Q2 and Q3 describe the capacitive behavior exhibited by the surface layer and electrode-electrolyte interface, respectively. Constant phase elements (expressed by Q) were used instead of pure capacitors to account for the non-ideal capacitive behavior of these components. The terms R3 and R4 subsequently represent the surface layer and charge-transfer resistance, respectively. The bulk electrode phenomena are described by W3 and C4. W3 is the Warburg component which is used to determine the Li diffusivity, while C4 represents the intercalation capacitance in the electrode. R2 was included in parallel to entire circuit to account for resistances generated by parasitic side reactions in every region, as the samples were not subject to cycling prior to EIS[65].

3.9 Other Characterization Techniques

The nanotube morphology was observed via field-emission SEM (FEI Teneo) operating at 5 kV. Raman spectroscopy was completed with a Horiba Scientific LabRam HR Evolution spectrometer using a 442 He:Cd laser with signal accumulation of 30 s scans. After instrument calibration, the samples were scanned at room temperature with an incident laser power of 100 mW from 100-1000 cm^{-1}. Samples were viewed at a magnification of 100x and scattered light was collected with a thermoelectrically cooled Si CCD detector.

CHAPTER FOUR: RESULTS AND DISCUSSION

4.1 Computational Modeling Results

Computational modeling was first done to predict the electronic properties of anatase TiO_2 and the effects of oxygen and titanium vacancies. For the pristine anatase structure, the bandgap was found to be approximately 3.2 eV, which matches closely with what has been previously reported in literature via experiments and theoretical calculations (***Figure 4.1***)[81-85]. There were significant changes to the band structure after an oxygen atom was removed from the anatase supercell, which resulted in an oxygen vacancy concentration of 1.39%. The Fermi energy shifted into the conduction band, and a mid-gap state appeared about 0.8 eV below the conduction band. The Fermi energy shift and the development of a mid-gap state were expected, as previous literature has experimentally shown similar results[83, 86-87]. The new mid-gap state is indicative of Ti^{3+} defect states, which have developed due to the introduction of oxygen vacancies, and subsequently act as electron donors[82, 87]. These changes imply that electrical conductivity would increase for the oxygen-deficient case.

While oxygen-deficient anatase TiO_2 has been well-studied, there is little information on how Ti vacancies affect electronic properties; consequently, the same computational approach was used in the Ti vacancy case. A Ti atom was removed and 4 H^+ ions were inserted into the oxygen sites around the vacancy to stabilize it and more accurately represent the defects introduced during WV treatment. A defect concentration

of 2.77% was achieved upon the removal of a Ti atom from the supercell. The resulting band structure changes for Ti-deficient anatase were not as drastic compared to the introduction of an oxygen vacancy, but they were still significant. The Fermi energy shifted down into the valence band and a new band appeared less than 0.2 eV above the valence band. These changes suggest that a large concentration of Ti vacancies in TiO_2 will result in p-type semiconductor behavior. It was unclear from this result what kind of effect the predicted change to p-type behavior would have on the electrical conductivity compared to the pristine and oxygen-deficient cases.

Partial charge simulations were then conducted to further investigate defect influence on the electronic properties (*Figure 4.2*). The resulting partial charge models suggest that the presence of Ti vacancies may reduce the electrical conductivity. In the valence band, there appears to be a higher electron density when a Ti vacancy is present (*Figure 4.2c*) compared to pristine anatase. When an oxygen vacancy is present, there is a delocalization of electrons in the valence band (*Figure 4.2b*). The conduction band has a much higher density of electrons near the Ti atoms for the oxygen vacancy case (*Figure 4.2e*), but the electron density appears to decrease when a Ti vacancy is introduced (*Figure 4.2f*). This supports the suggestion that Ti vacancies would cause a slight decrease in electronic conductivity.

To validate the DFT simulation results, TiO_2 nanotubes were annealed in O_2, Ar, N_2, and WV at 450°C for 4 hours to generate the appropriate defects. The samples were then characterized via Mott-Schottky analysis to determine their charge carrier densities. Bode plots in the frequency range 100 kHz-100 mHz were first acquired to determine the frequency at which *Z'* becomes constant (*Figure A.1*). The plot for each atmosphere

indicated that *Z'* plateaus at a frequency of about 500 Hz; therefore, the curves at 1.3 kHz

were used to calculate the charge carrier density for each sample.

a)   b)   c)
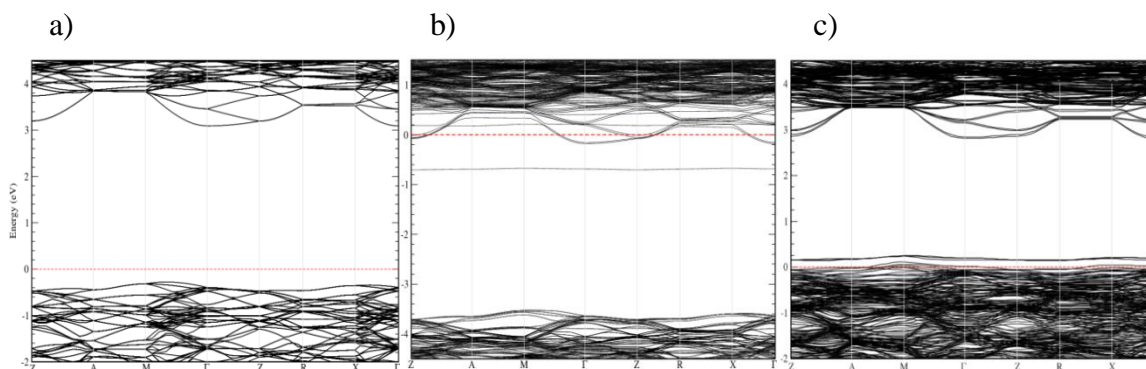
Figure 4.1   Band structures of a) pristine anatase TiO$_2$, b) anatase TiO$_2$ with O vacancy, and c) anatase TiO$_2$ with Ti vacancy
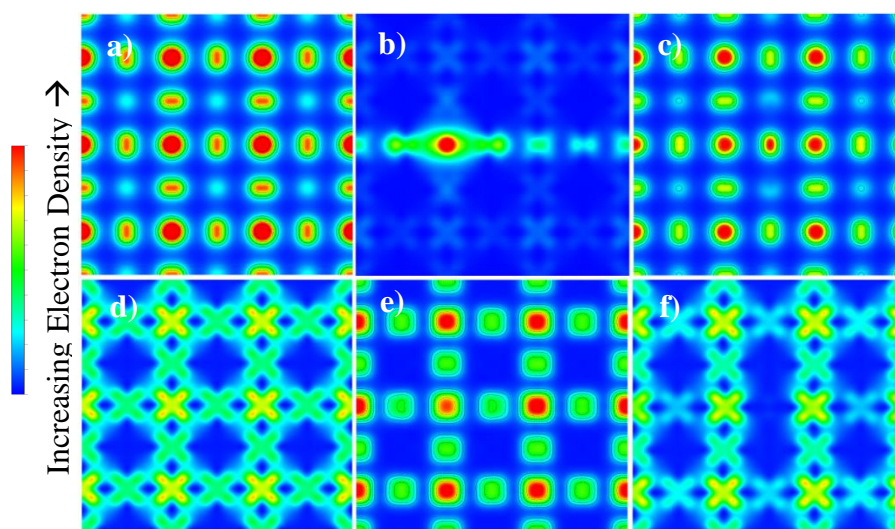
Figure 4.2   Partial charge models for pristine anatase TiO$_2$ (a & d), anatase TiO$_2$ with O vacancy (b & e), and anatase TiO$_2$ with Ti vacancy (c & f). Images a-c are the valence band models, d-f are the conduction band models

4.2 Mott-Schottky Analysis

From the Mott-Schottky plot at 1.3 kHz (***Figure 4.3***), the O$_2$- and WV-treated

samples have the steepest slopes, followed by the shallower plots of the Ar- and N$_2$-

treated samples. This correlates to the WV treatment causing the lowest carrier density,

while the N_2 treatment results in the largest carrier density (***Table 4.1***). These results seem to be in line with the computational models. Annealing under oxygen-deficient conditions should result in the generation of oxygen vacancies, which would result in the presence of more free electrons in the TiO_2 nanotube structure. All four Mott-Schottky plots have the profile associated with n-type semiconductor behavior[42]. This means that the charge carriers in these samples are electrons, which suggests an increase in their concentration would lead to a shallower slope in the plotted data.

The flat-band potential can also be obtained from the Mott-Schottky plots by finding the x-intercept of the tangent line to the linear region of each curve. This value corresponds to the amount of potential needed to eliminate band bending[88]. The slight positive shift of the flat-band potential for the oxygen-deficient treatments compared to the O_2-treated sample is another indicator that oxygen vacancies may have formed[46, 63].
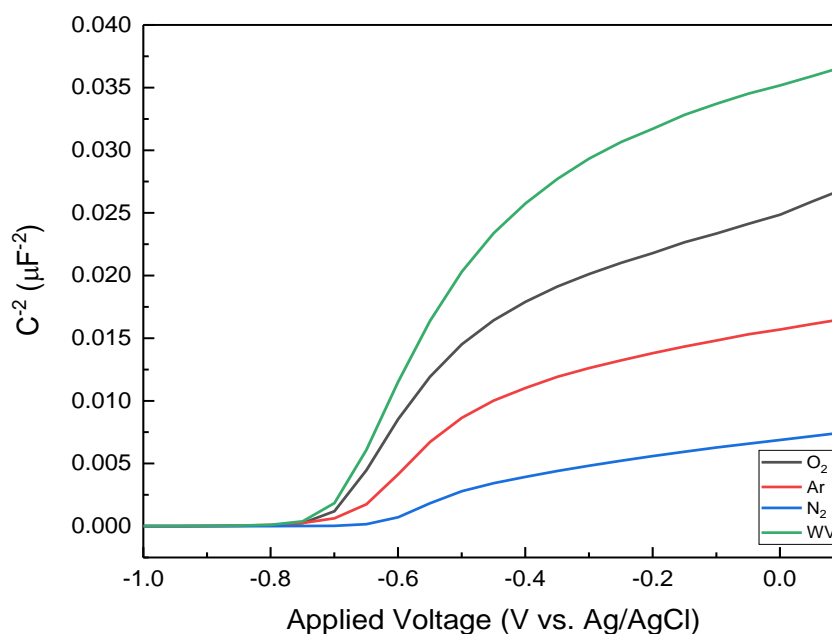
Figure 4.3   Mott-Schottky plots of anatase TiO_2 nanotubes annealed under different atmospheres

Table 4.1 **Charge carrier densities and flat-band potentials of anatase TiO$_2$ nanotubes annealed under different atmospheres**

Atmosphere	Charge Carrier Density (cm^{-3})	Flat-Band Potential (V)
O$_2$	2.01×10^{19}	-0.715
Ar	3.31×10^{19}	-0.688
N$_2$	8.06×10^{19}	-0.650
WV	1.49×10^{19}	-0.716

4.3 Two-Point Electrical Conductivity Results

Electrical conductivity measurements were conducted to supplement the conclusions drawn from the Mott-Schottky analysis. Using a two-point measurement, the out-of-plane conductivities of the annealed nanotubes were found (***Table 4.2***). The oxygen-deficient atmospheres increased conductivity, with the value for the N$_2$-treated sample changing by two orders of magnitude. In contrast, the WV treatment caused a decrease in conductivity. These results were consistent with the Mott-Schottky data, as changes in charge carrier density should correlate with the electrical conductivity. Our conductivities were also comparable with previously reported two-point measurements on anatase TiO$_2$ nanotubes[38, 71]. The conductivity measurements and Mott-Schottky analysis match up well with the theoretical models. The Ar and N$_2$ treatments increase the conductivity and charge carrier density of the anatase nanotubes, suggesting that the atmospheres have indeed created oxygen vacancies. On the other hand, the WV treatment displays a slight decrease in its electrical performance, which implies that Ti vacancies may have formed. This behavior is likely a consequence of the decreased electron density in the conduction band as evidenced by the partial charge models. The Ti vacancies may

act as electron acceptors and therefore prevent the electrons from participating in conduction[89].

It is interesting to note that the Ar-treated samples have lower conductivities and carrier densities compared to the N_2-treated samples. The variation in electrical conductivity as a result of the two different oxygen-deficient treatments may be due to their reactivity. Since Ar is a noble gas, it will not interact with any oxygen atoms that have been released from TiO_2. Any oxygen atoms that do not combine to form O_2 will likely reenter the TiO_2 structure. However, N_2 could form a variety of nitrogen oxides with the outgassed oxygen atoms, especially given the high annealing temperature. The consumption of additional oxygen atoms as a consequence of nitrogen oxide formation could explain the increase in oxygen vacancies and conductivity. Be that as it may, further research would have to be conducted to verify this proposed theory.

Table 4.2   Out-of-plane electrical conductivity of TiO$_2$ nanotubes annealed under different atmospheres

Atmosphere	Electrical Conductivity (S/m)
O_2	3.28×10^{-2}
Ar	6.86×10^{-2}
N_2	1.41
WV	6.33×10^{-3}

4.4 SEM and XRD Results

Additional characterization techniques were used to determine the morphological and crystallographic effects of the heat treatments as well as to further confirm the presence of the generated point defects. SEM images of the TiO_2 nanotubes after treatment show that the nanotubes maintain their structural integrity regardless of annealing conditions, with an average tube diameter of approximately 30 nm, tube wall

thickness of about 10 nm, and tube height of 2 μm (***Figure 4.4 and A.2***). Each of the
annealed samples was subsequently characterized using XRD. As expected, the resulting
XRD patterns for each sample matched well with anatase TiO_2 (***Figure 4.5***). Strong Ti
peaks were also present due to the Ti substrate. In addition, weak rutile (110) peaks were
present for the O_2 and WV samples, but not for the Ar or N_2 samples, which is consistent
with previous reports on the inhibition of anatase-rutile transformation in oxygen-
deficient environments[36, 40, 48, 63]. Upon refining the XRD patterns, there were no
significant changes in the unit cell parameters for samples annealed in different
atmospheres compared to the O_2 control sample. This result suggests that the effects of
defect formation on the crystallographic structure of the TiO_2 nanotubes were too small
to measure.

The XRD patterns were also used to generate Williamson-Hall plots to calculate
the microstrain present in each of the annealed samples (***Figure A.3***). As shown in
Equation 3.1, the slope of the trendline fitted to the data corresponds directly with the
strain in the sample. These plots revealed that the microstrain for all of the samples was
negligible as the slope of each trendline was extremely small (***Table A.3***). Since
microstrain is considered negligible, only the crystallite size of the nanotubes contributes
to the FWHM of the XRD pattern peaks. Under this assumption, the crystallite size for
the samples was calculated using ***Equation 3.2*** to be about 39-48 nm (***Table A.3***).
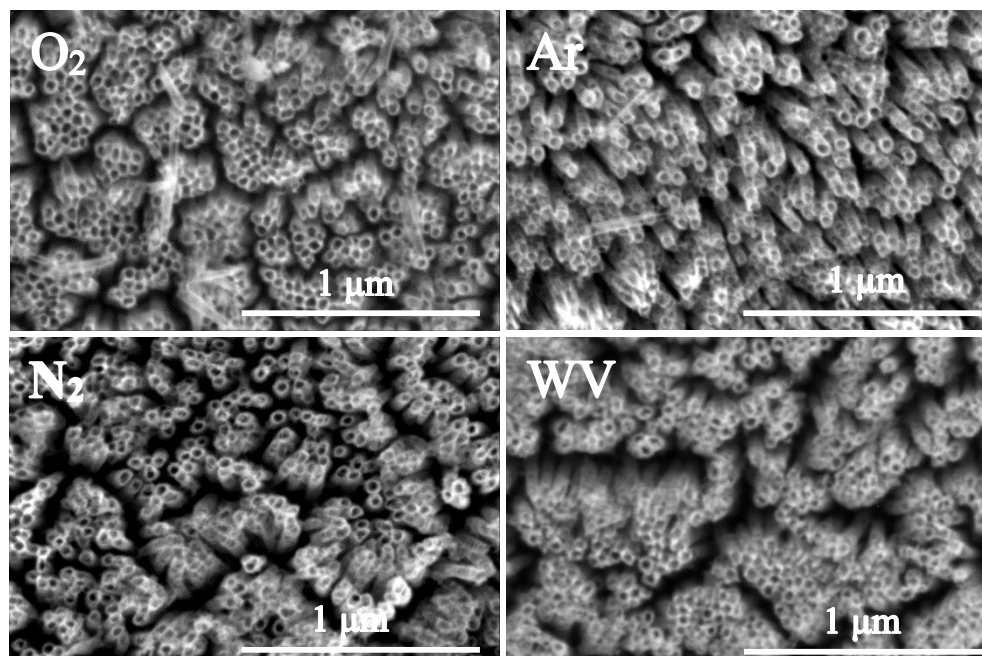
Figure 4.4   SEM images of anatase TiO₂ nanotubes annealed under different atmospheres.
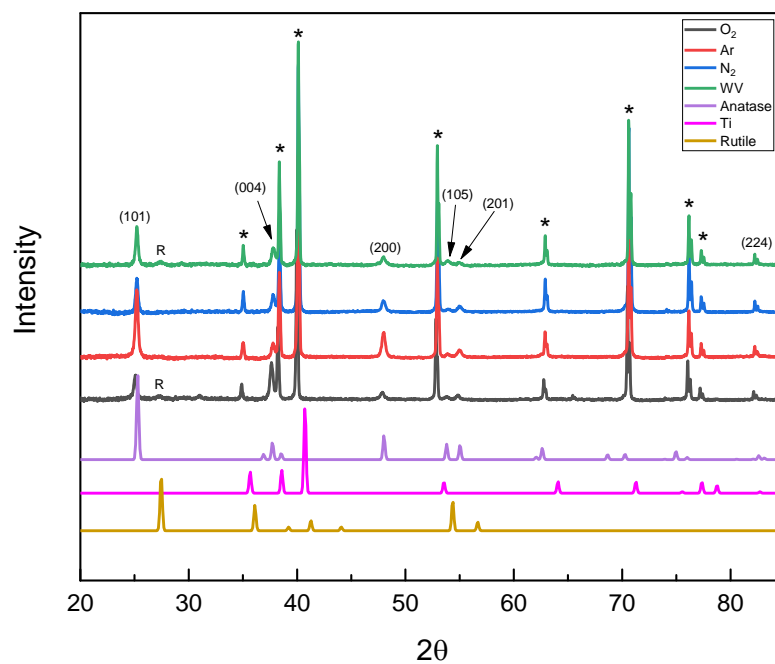
Figure 4.5   XRD spectra of anatase TiO₂ nanotubes annealed under different atmospheres. R indicates rutile (110) peak. * indicates metallic Ti peak.

4.5 Raman Spectroscopy Results

The annealed samples were also characterized using Raman spectroscopy (***Figure 4.6***). Each sample clearly had the associated spectrum for anatase TiO_2, with peaks present at approximately 144 cm^{-1}, 395 cm^{-1}, 517 cm^{-1}, and 636 cm^{-1}. The peaks correspond to the $E_g(1)$, $B_{1g}(1)$, $B_{1g}(2)+A_{1g}$, and $E_g(3)$ vibrational modes, respectively[38, 90-92]. A small peak at 196 cm^{-1} associated with the $E_g(2)$ vibrational mode was also present in all four samples[90, 92]. The $E_g(1)$, $E_g(2)$, and $B_{1g}(1)$ peaks correspond to O-Ti-O bending modes, while the $B_{1g}(2)+A_{1g}$ and $E_g(3)$ peaks correspond to Ti-O stretching modes[90]. As seen in ***Figure 4.6***, there are some differences in the annealed samples compared to the O_2 control case. The N_2 sample has a slight blueshift of the $E_g(1)$ peak of about 1.77 cm^{-1}, in addition to some peak broadening of about 1.32 cm^{-1}. Its $B_{1g}(1)$ and $E_g(3)$ peaks also have some broadening (***Tables A.1 and A.2***). Phonon confinement, strain, and nonstoichiometry could all contribute to the development of the observed blueshift and broadening[91-96]. Dispersion caused by phonons will occur if the TiO_2 crystallite size is less than 10-20 nm[38, 51, 91]. However, as discussed in Section 4.4, the crystallite size for all of the samples is 39-48 nm, which eliminates the possibility of phonon confinement. The Williamson-Hall plots (***Figure A.3***) also demonstrated that microstrain is negligible for each annealed sample. Thus, it is most probable that the observed changes in the $E_g(1)$ mode are due to the formation and proliferation of oxygen vacancies. Similar results have been reported in a number of studies on non-stoichiometric TiO_2 nanostructures[38, 51, 96-97]. Furthermore, the observed Raman shift for the N_2 sample is also in agreement with the computational models and enhanced electrical conductivity.
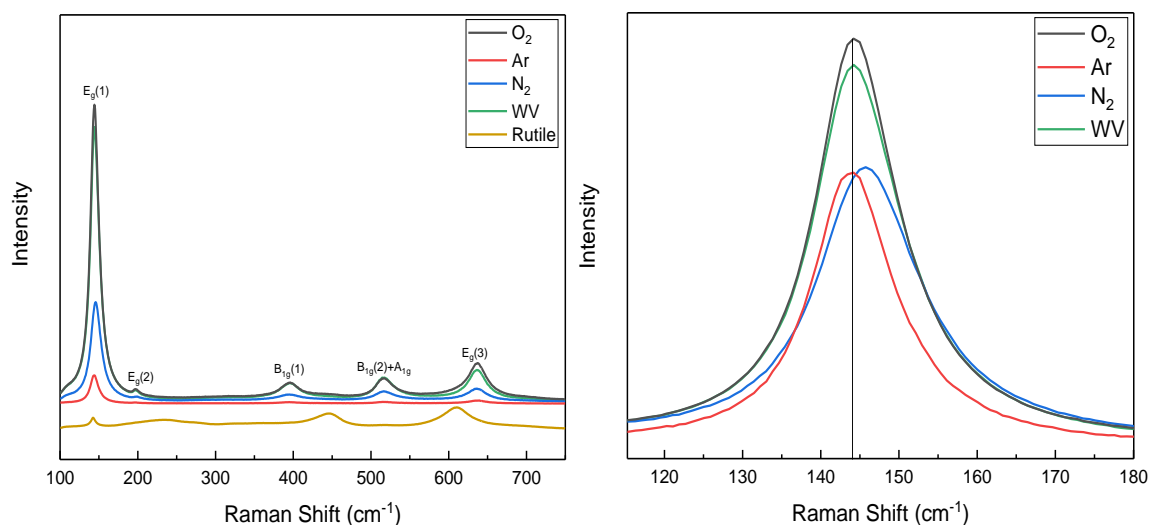
Figure 4.6   a) Raman spectra of anatase TiO$_2$ nanotubes annealed under different atmospheres with rutile spectrum for comparison. b) Normalized Raman spectra of E$_g$(1) vibrational mode for anatase TiO$_2$ nanotubes annealed under different atmospheres

The samples annealed in Ar and WV have negligible peak shift and broadening for all vibrational modes (*Figure A.4*). This is expected for the WV sample, as no oxygen vacancies are expected to form. It is also suggests that the Ti vacancy concentration is not large enough to have an effect on the Raman spectrum of anatase TiO$_2$. The lack of peak shift is slightly surprising in the case of Ar, as it is also an oxygen-deficient atmosphere; however, the lower concentration of O vacancies for the Ar-treated sample may be responsible for the lack of E$_g$(1) blueshift. This result is also consistent with the electrical conductivity and Mott-Schottky measurements. It should be noted that the N$_2$ and Ar samples have lower peak intensities compared to the O$_2$ and WV samples. While this decrease in intensity could indicate some disorder due to defect generation, it is also possible that the intensity varied due to the spot-like nature of Raman characterizations. Spots with lower tube density or thinner regions of TiO$_2$ would result in these intensity

drops. However, the peak intensity drop was consistent across the Ar- and N_2-treated samples and therefore can be trusted as an indicator of crystallinity loss.

4.6 Electrochemical Results

4.6.1 Low Rate Performance

The annealed samples were used as anodes in lithium-ion batteries to determine their electrochemical properties. The O_2-treated control sample displayed an initial charge of 197.6 mAh/g, which stabilized to 186.9 mAh/g after 30 cycles (*Figure 4.7*). Capacity data of the control sample were consistent with previously reported values for anatase TiO_2 nanotubes in Li-ion batteries[26, 98-99]. There was a marked increase in specific capacity when the anode material was annealed in oxygen-deficient environments. The initial charge capacity for the Ar-treated sample was 218.0 mAh/g which decreased to 206.4 mAh/g after 30 cycles, while the N_2-treated sample had an initial charge capacity of 246.6 mAh/g and 232.7 mAh/g after 30 cycles. The WV-treated sample exhibited a similar increase in capacity to the N_2 sample. The initial charge capacity increased to 246.5 mAh/g and was 231.3 mAh/g after 30 cycles. The Coulombic efficiency (ratio between the charge and discharge capacity) after 30 cycles for all atmospheric treatments was fairly consistent, as the values for O_2 control, Ar, N_2, and WV were 98.8, 97.7, 98.1, and 97.1%, respectively.
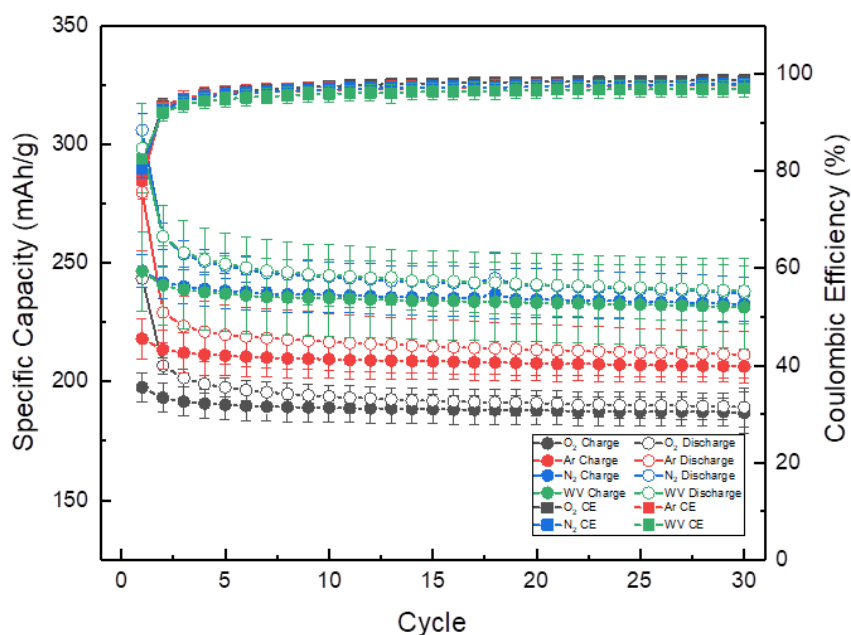
Figure 4.7   **Specific capacities of anatase TiO$_2$ nanotubes annealed under different atmospheres. Cells were cycled from 0.9 to 2.5 V at a theoretical C rate of C/20**

The improved electrical conductivity displayed by the nanotubes due to the generation of oxygen vacancies in the Ar- and N$_2$-treated samples facilitated an increase in capacity. The disparity between the Ar- and N$_2$-treated samples is still present, as the N$_2$ treatment has a significantly higher capacity compared to its oxygen-deficient counterpart. This difference is consistent with the conductivity measurements and gives additional support to the claim that annealing under Ar generates fewer oxygen vacancies compared to N$_2$. It is important to note that the WV treatment resulted in capacity comparable to the N$_2$ treatment. This indicates that the slight decrease in electrical conductivity, which would be expected to have a detrimental effect on battery performance, may be compensated by the increase of Li$^+$ ion intercalation sites provided by the Ti vacancies; therefore, the results of these experiments suggest that the electronic

conductivity of the electrode materials is not necessarily indicative of electrochemical performance.

4.6.2 Voltage Profiles and dQ/dV Plots

The voltage profiles were then studied to determine whether there were any fundamental differences in electrochemical behavior (***Figure 4.8***). The shape of the voltage profiles and dQ/dV plots were quite similar for each of the atmospheric treatments. This was expected, as there were no significant changes in crystallographic structure (as evidenced by the Raman and XRD spectra) due to different annealing environments. For all samples, a wide discharge plateau begins at about 1.78 V, which is followed by a much smaller plateau at approximately 1.5 V. The charge profile displays a change of slope near 1.6 V and its wide plateau region begins at approximately 1.87 V. The plateau regions for the charge and discharge profiles are consistent with the Li deintercalation and intercalation potentials for anatase TiO_2[25-26, 98, 100-101]. The presence of these plateaus indicates the addition and removal of Li ions to and from the octahedral interstitial sites[25, 98, 101]. The onset of the wide discharge plateau at 1.78 V corresponds to the transition of Li-poor anatase TiO_2 to $Li_{0.5}TiO_2$ (*Imma*) and the following plateau at 1.5 V then describes the transition of $Li_{0.5}TiO_2$ to $LiTiO_2$ (*I4$_1$/amd*) with further lithium intercalation[102-104]. From the voltage profiles, it is apparent that the broadening of the anatase intercalation plateaus is responsible for the increase in capacity for the oxygen-deficient and WV atmospheres. The dQ/dV plots also correspond well to the voltage profiles (***Figure A.5***). One peak during charging was located at about 1.9 V with a faint plateau around 1.7 V, while two peaks were located at 1.5 and 1.75 V during discharge.
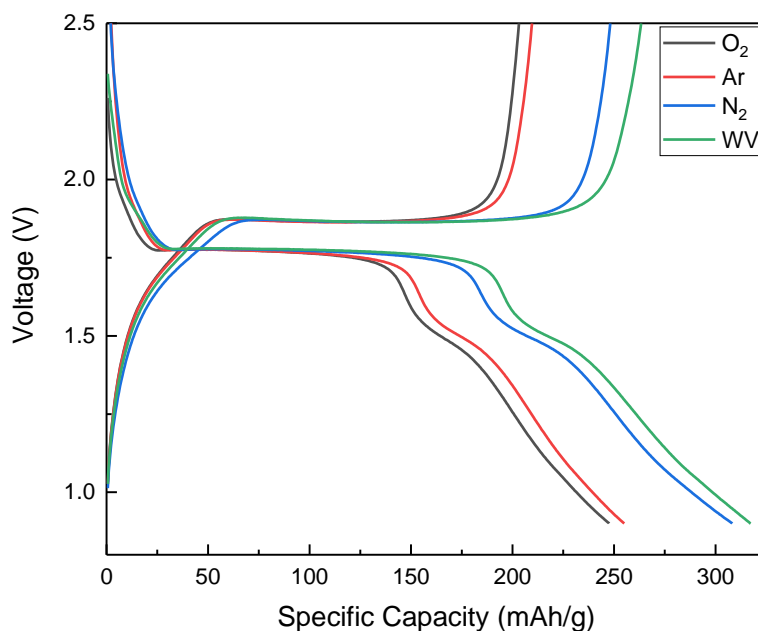
Figure 4.8   1st cycle voltage profiles of anatase TiO₂ nanotubes annealed under different atmospheres. Cells were cycled at a theoretical C rate of C/20

4.6.3 EIS Plots

Further characterizations were required to investigate the contradictory trends presented by the electrical conductivity measurements and electrochemical performance for the WV treatment. As a consequence, EIS was conducted to measure the Li diffusivity of the annealed samples (***Figure 4.9***). The equivalent circuit shown in ***Figure 3.9*** was used to fit the experimentally obtained data to obtain the Li diffusivity (***Table 4.3***). The calculated diffusivities were comparable to values already reported in literature[105-107]. From the fitting, it was found that the WV-treated sample had the largest Li diffusivity. The improvement of the Li diffusivity was particularly significant, as it was two orders of magnitude larger than the diffusivity of the O₂ control sample. The increased Li diffusivity helps justify the high specific capacity exhibited by the WV-

treated sample. While Ti vacancies created by the WV treatment decreased electrical

conductivity, their behavior as additional Li intercalation sites likely enabled the increase

of Li diffusivity.
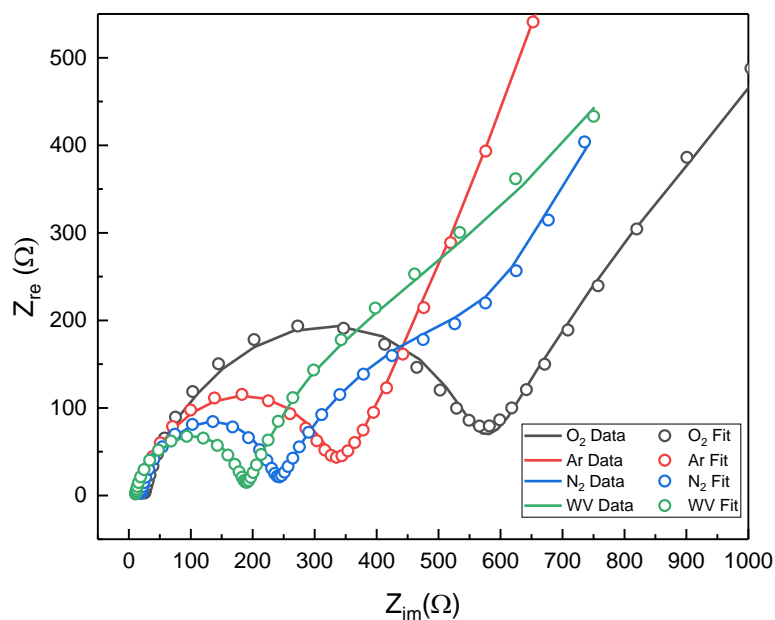
Figure 4.9   Nyquist plots of anatase TiO₂ nanotubes annealed under different atmospheres

Table 4.3   Lithium diffusivity values obtained from EIS data fitting for anatase TiO₂ nanotubes annealed in different atmospheres

Atmosphere	Li Diffusivity (cm^2/s)
O_2	2.20×10^{-13}
Ar	2.32×10^{-13}
N_2	4.30×10^{-12}
WV	1.04×10^{-11}

4.6.4 Rate Study

Rate studies were also conducted to determine how the formation of the oxygen and Ti vacancies would affect the electrochemical performance of the TiO_2 nanotubes at elevated current rates (*Figure 4.10*). At C/20 (1C rate: charge/discharge in 1 hour), the charge capacities for the N_2- and WV-treated samples were almost identical at 231.9 and 230.6 mAh/g, respectively. However, the performance began to change as the C rate was increased. At C/2, their behavior noticeably differed, as the N_2-treated sample had a charge capacity of 176.9 mAh/g, while the WV treatment had a lower capacity of 166.0 mAh/g. The most dramatic decrease in capacity occurred at the highest current rate of 5C. The N_2 treatment caused capacity to decrease to 103.5 mAh/g, but the WV-treated sample had its capacity drop sharply to 80.4 mAh/g, which was comparable to the O_2 control capacity of 80.5 mAh/g. The Ar-treated sample maintained its slightly higher capacity with respect to the control case at all C rates until 5C. All samples exhibited good capacity recovery after being subjected to the highest current rate. The results of the rate study suggest that the electrical conductivity of the samples plays a larger role in their performance at higher currents. The higher Li diffusivity in the WV-treated sample does not enable it to perform well at higher C rate, but the N_2-treated sample has adequate capacity at rates up to 5C. This indicates that larger electrical conductivity values are necessary to achieve high rate capability.
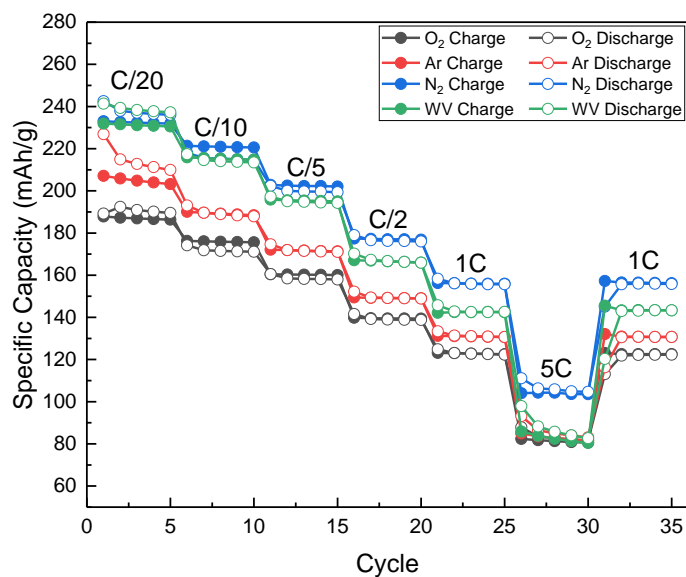
Figure 4.10   Rate study cycling at different C rates of anatase TiO₂ nanotubes annealed under different atmospheres.

CHAPTER FIVE: CONCLUSION

5.1 Final Conclusions

DFT simulations were used to predict the effect of defect formation on electrical conductivity. From the simulations, it was anticipated that oxygen vacancies would increase electrical conductivity as a likely consequence of the formation of a mid-gap state. Partial charge simulations indicated that a Ti vacancy stabilized by 4 H^+ ions would decrease electron concentration in the conduction band and possibly decrease electrical conductivity. These predictions were confirmed by Mott-Schottky analysis and two-point electrical conductivity measurements of anatase TiO_2 nanotube samples annealed in different atmospheres. Oxygen vacancies generated due to Ar or N_2 treatment caused the charge carrier density and electrical conductivity of the samples to increase. Ti vacancies stabilized via WV treatment resulted in a slight decrease of conductivity. The reported changes in electrical properties were strong indicators that the respective defects had indeed formed. These conclusions were supported by Raman spectroscopy. Raman spectroscopy of the N_2-treated sample displayed a blueshift and broadening of the $E_g(1)$ mode, which confirmed the formation of oxygen vacancies in the sample. Both oxygen and Ti vacancies caused an improvement in the specific capacity of the TiO_2 nanotubes when they were used as anodes in Li-ion batteries. The Ar- and N_2-treated samples had an increase in capacity of 10% and 25%, respectively, while the WV treatment resulted in a 24% capacity increase compared to the O_2 control case. The electrical conductivity

increase due to oxygen vacancy formation was expected to correlate with an increase in capacity, and the results were consistent with that prediction; however, the increase in capacity as a result of the WV treatment was surprising, particularly as there was a decrease in sample conductivity. To investigate this result further, EIS studies were conducted and revealed that the WV-treated sample had the largest Li diffusivity. The improved diffusivity of the WV-treated sample likely explains its capacity increase in spite of its lower electrical conductivity. Subsequent rate studies demonstrated that the N_2-treated sample had the best performance at high current rates of 5C. These results suggest that while high electrical conductivity may improve rate capability, it cannot be used as the only significant indicator of battery material performance.

5.2 Future Studies

Although this work addresses many questions posed by the original hypothesis, many aspects still require further investigation. More powerful characterization techniques such as positron annihilation lifetime spectroscopy should be conducted to obtain additional information about the defect concentration. Cycle life tests should also be done to determine if the presence of oxygen or titanium vacancies has an effect on the long-term stability of batteries. Cyclic voltammetry should be conducted to gather a more complete understanding of the kinetics occurring in the system during operation. In-situ XRD and TEM studies could be conducted to understand whether the oxygen and titanium vacancies impact the Li intercalation mechanism. Additional studies should also be conducted to understand the difference between the Ar and N_2 treatments. The mechanism of defect formation via each atmospheric treatment could also be studied.

Regardless of the conclusions found by this work, there is a wealth of information that

has yet to be understood concerning this topic.

REFERENCES

1.   Center for Climate and Energy Solutions Global Emissions. https://www.c2es.org/content/international-emissions/ (accessed 17 Mar).

2.   Environmental Protection Agency Climate Change Indicators: U.S. And Global Temperature. https://www.epa.gov/climate-indicators/climate-change-indicators-us-and-global-temperature#ref2 (accessed 12 Mar).

3.   Environmental Protection Agency Climate Change Indicators: Global Greenhouse Gas Emissions. https://www.epa.gov/climate-indicators/climate-change-indicators-global-greenhouse-gas-emissions#ref4 (accessed 15 Mar).

4.   Slater, M. D.; Kim, D.; Lee, E.; Johnson, C. S., Sodium-Ion Batteries. *Adv Funct Mater* **2013**, *23*, 947-958.

5.   Scrosati, B.; Garche, J., Lithium Batteries: Status, Prospects and Future. *J Power Sources* **2010**, *195*, 2419-2430.

6.   Etacheri, V.; Marom, R.; Elazari, R.; Salitra, G.; Aurbach, D., Challenges in the Development of Advanced Li-Ion Batteries: A Review. *Energ Environ Sci* **2011**, *4*, 3243-3262.

7.   Yabuuchi, N.; Kubota, K.; Dahbi, M.; Komaba, S., Research Development on Sodium-Ion Batteries. *Chem Rev* **2014**, *114*, 11636-11682.

8.   Osswald, P. J.; del Rosario, M.; Garche, J.; Jossen, A.; Hoster, H. E., Fast and Accurate Measurement of Entropy Profiles of Commercial Lithium-Ion Cells. *Electrochim Acta* **2015**, *177*, 270-276.

9.   Whittingham, M. S., History, Evolution, and Future Status of Energy Storage. *P Ieee* **2012**, *100*, 1518-1534.

10. Kubota, K.; Komaba, S., Review-Practical Issues and Future Perspective for Na-Ion Batteries. *J Electrochem Soc* **2015**, *162*, A2538-A2550.

11. Rahman, M. A.; Wang, X. J.; Wen, C., Enhanced Electrochemical Performance of Li-Ion Batteries with Nanoporous Titania as Negative Electrodes. *J Energy Chem* **2015**, *24*, 157-170.

12. Gao, R. M.; Jiao, Z.; Wang, Y.; Xu, L. Q.; Xia, S. S.; Zhang, H. J., Eco-Friendly Synthesis of Rutile Tio2 Nanostructures with Controlled Morphology for Efficient Lithium-Ion Batteries. *Chem Eng J* **2016**, *304*, 156-164.

13. Li, Y.; Song, J.; Yang, J., A Review on Structure Model and Energy System Design of Lithium-Ion Battery in Renewable Energy Vehicle. *Renew Sust Energ Rev* **2014**, *37*, 627-633.

14. Nishi, Y., Lithium Ion Secondary Batteries; Past 10 Years and the Future. *J Power Sources* **2001**, *100*, 101-106.

15. de las Casas, C.; Li, W., A Review of Application of Carbon Nanotubes for Lithium Ion Battery Anode Material. *J Power Sources* **2012**, *208*, 74-85.

16. Aurbach, D.; Markovsky, B.; Weissman, I.; Levi, E.; Ein-Eli, Y., On the Correlation between Surface Chemistry and Performance of Graphite Negative Electrodes for Li Ion Batteries. *Electrochim Acta* **1999**, *45*, 67-86.

17. Liu, Y.; Yang, Y. F., Recent Progress of Tio2-Based Anodes for Li Ion Batteries. *J Nanomater* **2016**.

18. Bresser, D.; Oschmann, B.; Tahir, M. N.; Mueller, F.; Lieberwirth, I.; Tremel, W.; Zentel, R.; Passerini, S., Carbon-Coated Anatase Tio2 Nanotubes for Li- and Na-Ion Anodes. *J Electrochem Soc* **2015**, *162*, A3013-A3020.

19. Bresser, D., et al., Transforming Anatase Tio2 Nanorods into Ultrafine Nanoparticles for Advanced Electrochemical Performance. *J Power Sources* **2015**, *294*, 406-413.

20. Deng, D.; Kim, M. G.; Lee, J. Y.; Cho, J., Green Energy Storage Materials: Nanostructured Tio2 and Sn-Based Anodes for Lithium-Ion Batteries. *Energ Environ Sci* **2009**, *2*, 818-837.

21. Lee, K.; Mazare, A.; Schmuki, P., One-Dimensional Titanium Dioxide Nanomaterials: Nanotubes. *Chem Rev* **2014**, *114*, 9385-9454.

22. Fehse, M.; Ventosa, E., Is Tio2(B) the Future of Titanium-Based Battery Materials? *Chempluschem* **2015**, *80*, 785-795.

23. Panda, S. K.; Yoon, Y.; Jung, H. S.; Yoon, W. S.; Shin, H., Nanoscale Size Effect of Titania (Anatase) Nanotubes with Uniform Wall Thickness as High Performance Anode for Lithium-Ion Secondary Battery. *J Power Sources* **2012**, *204*, 162-167.

24. Zakharova, G. S.; Jahne, C.; Popa, A.; Taschner, C.; Gemming, T.; Leonhardt, A.; Buchner, B.; Klingeler, R., Anatase Nanotubes as an Electrode Material for Lithium-Ion Batteries. *J Phys Chem C* **2012**, *116*, 8714-8720.

25. Ryu, W. H.; Nam, D. H.; Ko, Y. S.; Kim, R. H.; Kwon, H. S., Electrochemical Performance of a Smooth and Highly Ordered Tio2 Nanotube Electrode for Li-Ion Batteries. *Electrochim Acta* **2012**, *61*, 19-24.

26. Kim, J.; Cho, J., Rate Characteristics of Anatase Tio2 Nanotubes and Nanorods for Lithium Battery Anode Materials at Room Temperature. *J Electrochem Soc* **2007**, *154*, A542-A546.

27. Qi, Y.; Harris, S. J., In Situ Observation of Strains During Lithiation of a Graphite Electrode. *J Electrochem Soc* **2010**, *157*, A741-A747.

28. Li, Y.; Luo, J. D.; Hu, X. Y.; Wang, X. F.; Liang, J. C.; Yu, K. F., Fabrication of Tio2 Hollow Nanostructures and Their Application in Lithium Ion Batteries. *J Alloy Compd* **2015**, *651*, 685-689.

29. Roy, P.; Berger, S.; Schmuki, P., Tio2 Nanotubes: Synthesis and Applications. *Angew Chem Int Edit* **2011**, *50*, 2904-2939.

30. Lakshmi, B. B.; Dorhout, P. K.; Martin, C. R., Sol-Gel Template Synthesis of Semiconductor Nanostructures. *Chem Mater* **1997**, *9*, 857-862.

31. Kasuga, T.; Hiramatsu, M.; Hoson, A.; Sekino, T.; Niihara, K., Formation of Titanium Oxide Nanotube. *Langmuir* **1998**, *14*, 3160-3163.

32. Kasuga, T.; Hiramatsu, M.; Hoson, A.; Sekino, T.; Niihara, K., Titania Nanotubes Prepared by Chemical Processing. *Adv Mater* **1999**, *11*, 1307-+.

33. Smith, K. A., et al., Effects of Proton Irradiation on Structural and Electrochemical Charge Storage Properties of Tio2 Nanotube Electrodes for Lithium-Ion Batteries. *J Mater Chem A* **2017**, *5*, 11815-11824.

34. Uberuaga, B. P.; Bai, X. M., Defects in Rutile and Anatase Polymorphs of Tio2: Kinetics and Thermodynamics near Grain Boundaries. *J Phys-Condens Mat* **2011**, *23*.

35. Hahn, B. P.; Long, J. W.; Mansour, A. N.; Pettigrew, K. A.; Osofsky, M. S.; Rolison, D. R., Electrochemical Li-Ion Storage in Defect Spinel Iron Oxides: The Critical Role of Cation Vacancies. *Energ Environ Sci* **2011**, *4*, 1495-1502.

36. Liu, S. J.; Ma, Q.; Gao, F.; Song, S. H.; Gao, S., Relationship between N-Doping Induced Point Defects by Annealing in Ammonia and Enhanced Thermal Stability for Anodized Titania Nanotube Arrays. *J Alloy Compd* **2012**, *543*, 71-78.

37. Wang, G. M.; Yang, Y.; Han, D. D.; Li, Y., Oxygen Defective Metal Oxides for Energy Conversion and Storage. *Nano Today* **2017**, *13*, 23-39.

38. Liao, A. Z.; Wang, C. W.; Chen, J. B.; Zhang, X. Q.; Li, Y.; Wang, J., Remarkably Improved Field Emission of Tio2 Nanotube Arrays by Annealing Atmosphere Engineering. *Mater Res Bull* **2015**, *70*, 988-994.

39. Xiao, P.; Liu, D. W.; Garcia, B. B.; Sepehri, S.; Zhang, Y. H.; Cao, G. Z., Electrochemical and Photoelectrical Properties of Titania Nanotube Arrays Annealed in Different Gases. *Sensor Actuat B-Chem* **2008**, *134*, 367-372.

40. Hyam, R. S.; Lee, J.; Cho, E.; Khim, J.; Lee, H., Effect of Annealing Environments on Self-Organized Tio2 Nanotubes for Efficient Photocatalytic Applications. *J Nanosci Nanotechno* **2012**, *12*, 8908-8912.

41. Qiu, J. X.; Li, S.; Gray, E.; Liu, H. W.; Gu, Q. F.; Sun, C. H.; Lai, C.; Zhao, H. J.; Zhang, S. Q., Hydrogenation Synthesis of Blue Tio2 for High-Performance Lithium-Ion Batteries. *J Phys Chem C* **2014**, *118*, 8824-8830.

42. Lu, X. H.; Wang, G. M.; Zhai, T.; Yu, M. H.; Gan, J. Y.; Tong, Y. X.; Li, Y., Hydrogenated Tio2 Nanotube Arrays for Supercapacitors. *Nano Lett* **2012**, *12*, 1690-1696.

43. Zhang, M. H.; Yin, K. B.; Hood, Z. D.; Bi, Z. H.; Bridges, C. A.; Dai, S.; Meng, Y. S.; Paranthaman, M. P.; Chi, M. F., In Situ Tem Observation of the Electrochemical Lithiation of N-Doped Anatase Tio2 Nanotubes as Anodes for Lithium-Ion Batteries. *J Mater Chem A* **2017**, *5*, 20651-20657.

44. Alivov, Y.; Fan, Z. Y.; Johnstone, D., Titanium Nanotubes Grown by Titanium Anodization. *J Appl Phys* **2009**, *106*.

45. Macak, J. M.; Tsuchiya, H.; Schmuki, P., High-Aspect-Ratio Tio2 Nanotubes by Anodization of Titanium. *Angew Chem Int Edit* **2005**, *44*, 2100-2102.

46. Su, T.; Yang, Y. L.; Na, Y.; Fan, R. Q.; Li, L.; Wei, L. G.; Yang, B.; Cao, W. W., An Insight into the Role of Oxygen Vacancy in Hydrogenated Tio2 Nanocrystals in the Performance of Dye-Sensitized Solar Cells. *Acs Appl Mater Inter* **2015**, *7*, 3754-3763.

47. Koo, B.; Xiong, H.; Slater, M. D.; Prakapenka, V. B.; Baasubramanian, M.; Podsiadlo, P.; Johnson, C. S.; Rajh, T.; Shevchenko, E. V., Hollow Iron Oxide Nanoparticles for Application in Lithium Ion Batteries. *Nano Lett* **2012**, *12*, 2429-2435.

48. Liu, D. W.; Xiao, P.; Zhang, Y. H.; Garcia, B. B.; Zhang, Q. F.; Guo, Q.; Champion, R.; Cao, G. Z., Tio2 Nanotube Arrays Annealed in N2 for Efficient Lithium-Ion Intercalation. *J Phys Chem C* **2008**, *112*, 11175-11180.

49. Wang, G. M.; Wang, H. Y.; Ling, Y. C.; Tang, Y. C.; Yang, X. Y.; Fitzmorris, R. C.; Wang, C. C.; Zhang, J. Z.; Li, Y., Hydrogen-Treated Tio2 Nanowire Arrays for Photoelectrochemical Water Splitting. *Nano Lett* **2011**, *11*, 3026-3033.

50. Ghicov, A.; Tsuchiya, H.; Macak, J. M.; Schmuki, P., Annealing Effects on the Photoresponse of Tio2 Nanotubes. *Phys Status Solidi A* **2006**, *203*, R28-R30.

51. Salari, M.; Konstantinov, K.; Liu, H. K., Enhancement of the Capacitance in Tio2 Nanotubes through Controlled Introduction of Oxygen Vacancies. *J Mater Chem* **2011**, *21*, 5128-5133.

52. Hanzu, I.; Djenizian, T.; Knauth, P., Electrical and Point Defect Properties of Tio2 Nanotubes Fabricated by Electrochemical Anodization. *J Phys Chem C* **2011**, *115*, 5989-5996.

53. Xiong, H., et al., Compositional Tuning of Structural Stability of Lithiated Cubic Titania Via a Vacancy-Filling Mechanism under High Pressure. *Phys Rev Lett* **2013**, *110*.

54. Swider-Lyons, K. E.; Love, C. T.; Rolison, D. R., Improved Lithium Capacity of Defective V2o5 Materials. *Solid State Ionics* **2002**, *152*, 99-104.

55. Hahn, B. P.; Long, J. W.; Rolison, D. R., Something from Nothing: Enhancing Electrochemical Charge Storage with Cation Vacancies. *Accounts Chem Res* **2013**, *46*, 1181-1191.

56. McKeown, D. A.; Hagans, P. L.; Carette, L. P. L.; Russell, A. E.; Swider, K. E.; Rolison, D. R., Structure of Hydrous Ruthenium Oxides: Implications for Charge Storage. *J Phys Chem B* **1999**, *103*, 4825-4832.

57. Cross, A.; Morel, A.; Cormie, A.; Hollenkamp, T.; Donne, S., Enhanced Manganese Dioxide Supercapacitor Electrodes Produced by Electrodeposition. *J Power Sources* **2011**, *196*, 7847-7853.

58. Roh, B.; Macdonald, D. D., Defect Properties of Anodic Oxide Films on Titanium and Impact of Oxygen Vacancy on Oxygen Electrode Reactions.

http://etda.libraries.psu.edu/theses/approved/WorldWideIndex/ETD-1878/index.html.

59.   Baram, N.; Ein-Eli, Y., Electrochemical Impedance Spectroscopy of Porous Tio2 for Photocatalytic Applications. *J Phys Chem C* **2010**, *114*, 9781-9790.

60.   Tang, H.; Prasad, K.; Sanjines, R.; Schmid, P. E.; Levy, F., Electrical and Optical-Properties of Tio2 Anatase Thin-Films. *J Appl Phys* **1994**, *75*, 2042-2047.

61.   Islam, S. Z.; Reed, A.; Wanninayake, N.; Kim, D. Y.; Rankin, S. E., Remarkable Enhancement of Photocatalytic Water Oxidation in N-2/Ar Plasma Treated, Mesoporous Tio2 Films. *J Phys Chem C* **2016**, *120*, 14069-14081.

62.   Tsui, L. K.; Zangari, G., Water Content in the Anodization Electrolyte Affects the Electrochemical and Electronic Transport Properties of Tio2 Nanotubes: A Study by Electrochemical Impedance Spectroscopy. *Electrochim Acta* **2014**, *121*, 203-209.

63.   Mahajan, V. K.; Misra, M.; Raja, K. S.; Mohapatra, S. K., Self-Organized Tio2 Nanotubular Arrays for Photoelectrochemical Hydrogen Generation: Effect of Crystallization and Defect Structures. *J Phys D Appl Phys* **2008**, *41*.

64.   Levi, M. D.; Salitra, G.; Markovsky, B.; Teller, H.; Aurbach, D.; Heider, U.; Heider, L., Solid-State Electrochemical Kinetics of Li-Ion Intercalation into Li1-Xcoo2: Simultaneous Application of Electroanalytical Techniques Sscv, Pitt, and Eis. *J Electrochem Soc* **1999**, *146*, 1279-1289.

65.   Aurbach, D.; Levi, M. D.; Levi, E.; Teller, H.; Markovsky, B.; Salitra, G.; Heider, U.; Heider, L., Common Electroanalytical Behavior of Li Intercalation Processes into Graphite and Transition Metal Oxides. *J Electrochem Soc* **1998**, *145*, 3024-3034.

66.   Aurbach, D., Review of Selected Electrode-Solution Interactions Which Determine the Performance of Li and Li Ion Batteries. *J Power Sources* **2000**, *89*, 206-218.

67. Bard, A. J.; Faulkner, L. R., *Electrochemical Methods Fundamentals and Applications*, 2nd ed.; John Wiley & Sons, 2001.

68. Yan, Z. C.; Liu, L.; Tan, J. L.; Zhou, Q.; Huang, Z. F.; Xia, D. D.; Shu, H. B.; Yang, X. K.; Wang, X. Y., One-Pot Synthesis of Bicrystalline Titanium Dioxide Spheres with a Core-Shell Structure as Anode Materials for Lithium and Sodium Ion Batteries. *J Power Sources* **2014**, *269*, 37-45.

69. Shu, H. B., et al., The Effect of Ammonia Concentration on the Morphology and Electrochemical Properties of Lifepo4 Synthesized by Ammonia Assisted Hydrothermal Route. *Electrochim Acta* **2012**, *76*, 120-129.

70. Tighineanu, A. Electrical Conductivity of Tio2 Nanotubes. Friedrich-Alexander Universitat Erlangen-Nurnberg, 2014.

71. Tighineanu, A.; Ruff, T.; Albu, S.; Hahn, R.; Schmuki, P., Conductivity of Tio2 Nanotubes: Influence of Annealing Time and Temperature. *Chem Phys Lett* **2010**, *494*, 260-263.

72. Takeuchi, M.; Itoh, T.; Nagasaka, H., Dielectric Properties of Sputtered Tio2 Films. *Thin Solid Films* **1978**, *51*, 83-88.

73. Kresse, G.; Furthmuller, J., Efficient Iterative Schemes for Ab Initio Total-Energy Calculations Using a Plane-Wave Basis Set. *Phys Rev B* **1996**, *54*, 11169-11186.

74. Perdew, J. P.; Burke, K.; Ernzerhof, M., Generalized Gradient Approximation Made Simple. *Phys Rev Lett* **1996**, *77*, 3865-3868.

75. Liechtenstein, A. I.; Anisimov, V. I.; Zaanen, J., Density-Functional Theory and Strong-Interactions - Orbital Ordering in Mott-Hubbard Insulators. *Phys Rev B* **1995**, *52*, R5467-R5470.

76. Sinha, N. N.; Burns, J. C.; Sanderson, R. J.; Dahn, J., Comparative Studies of Hardware Corrosion at High Potentials in Coin-Type Cells with Non Aqueous Electrolytes. *J Electrochem Soc* **2011**, *158*, A1400-A1403.

77. Williamson, G. K.; Hall, W. H., X-Ray Line Broadening from Filed Aluminium and Wolfram. *Acta Metall Mater* **1953**, *1*, 22-31.

78. Vijayan, B.; Dimitrijevic, N. M.; Rajh, T.; Gray, K., Effect of Calcination Temperature on the Photocatalytic Reduction and Oxidation Processes of Hydrothermally Synthesized Titania Nanotubes. *J Phys Chem C* **2010**, *114*, 12994-13002.

79. Yam, F. K.; Beh, K. P.; Ng, W.; Hassan, Z., The Effects of Morphological Changes on the Vibrational Properties of Self-Organized Tio2 Nanotubes. *Thin Solid Films* **2011**, *520*, 807-812.

80. Scherrer, P., Bestimmung Der Grösse Und Der Inneren

Struktur Von Kolloidteilchen Mittels Röntgenstrahlen. *Göttinger Nachrichten Math. Phys.* **1918**, *2*, 98-100.

81. Landmann, M.; Rauls, E.; Schmidt, W. G., The Electronic Structure and Optical Response of Rutile, Anatase and Brookite Tio2. *J Phys-Condens Mat* **2012**, *24*.

82. Lin, Z. S.; Orlov, A.; Lambert, R. M.; Payne, M. C., New Insights into the Origin of Visible Light Photocatalytic Activity of Nitrogen-Doped and Oxygen-Deficient Anatase Tio2. *J Phys Chem B* **2005**, *109*, 20948-20952.

83. Nakamura, I.; Negishi, N.; Kutsuna, S.; Ihara, T.; Sugihara, S.; Takeuchi, E., Role of Oxygen Vacancy in the Plasma-Treated Tio2 Photocatalyst with Visible Light Activity for No Removal. *J Mol Catal a-Chem* **2000**, *161*, 205-212.

84. Phattalung, S. N.; Limpijumnong, S.; Yu, J., Passivated Co-Doping Approach to Bandgap Narrowing of Titanium Dioxide with Enhanced Photocatalytic Activity. *Appl Catal B-Environ* **2017**, *200*, 1-9.

85. Livraghi, S.; Paganini, M. C.; Giamello, E.; Selloni, A.; Di Valentin, C.; Pacchioni, G., Origin of Photoactivity of Nitrogen-Doped Titanium Dioxide under Visible Light. *J Am Chem Soc* **2006**, *128*, 15666-15671.

86. Dong, F.; Zhao, W. R.; Wu, Z. B.; Guo, S., Band Structure and Visible Light Photocatalytic Activity of Multi-Type Nitrogen Doped Tio2 Nanoparticles Prepared by Thermal Decomposition. *J Hazard Mater* **2009**, *162*, 763-770.

87. Sanjines, R.; Tang, H.; Berger, H.; Gozzo, F.; Margaritondo, G.; Levy, F., Electronic-Structure of Anatase Tio2 Oxide. *J Appl Phys* **1994**, *75*, 2945-2951.

88. Gelderman, K.; Lee, L.; Donne, S. W., Flat-Band Potential of a Semiconductor: Using the Mott-Schottky Equation. *J Chem Educ* **2007**, *84*, 685-688.

89. Na-Phattalung, S.; Smith, M. F.; Kim, K.; Du, M. H.; Wei, S. H.; Zhang, S. B.; Limpijumnong, S., First-Principles Study of Native Defects in Anatase Tio2. *Phys Rev B* **2006**, *73*.

90. Ohsaka, T.; Izumi, F.; Fujiki, Y., Raman-Spectrum of Anatase Tio2. *J Raman Spectrosc* **1978**, *7*, 321-324.

91. Georgescu, D.; Baia, L.; Ersen, O.; Baia, M.; Simon, S., Experimental Assessment of the Phonon Confinement in Tio2 Anatase Nanocrystallites by Raman Spectroscopy. *J Raman Spectrosc* **2012**, *43*, 876-883.

92. Sahoo, S.; Arora, A. K.; Sridharan, V., Raman Line Shapes of Optical Phonons of Different Symmetries in Anatase Tio2 Nanocrystals. *J Phys Chem C* **2009**, *113*, 16927-16933.

93. Swamy, V.; Kuznetsov, A.; Dubrovinsky, L. S.; Caruso, R. A.; Shchukin, D. G.; Muddle, B. C., Finite-Size and Pressure Effects on the Raman Spectrum Nanocrystalline Anatase Tio2. *Phys Rev B* **2005**, *71*.

94. Parker, J. C.; Siegel, R. W., Raman Microprobe Study of Nanophase Tio2 and Oxidation-Induced Spectral Changes. *J Mater Res* **1990**, *5*, 1246-1252.

95. Parker, J. C.; Siegel, R. W., Calibration of the Raman-Spectrum to the Oxygen Stoichiometry of Nanophase Tio2. *Appl Phys Lett* **1990**, *57*, 943-945.

96. Scepanovic, M. J.; Grujic-Brojcin, M. U.; Dohcevic-Mitrovic, Z. D.; Popovic, Z. V., Effects of Confinement, Strain and Nonstoichiometry on Raman Spectra of Anatase Tio2 Nanopowders. *Mater Sci Forum* **2006**, *518*, 101-106.

97. Wang, J. G.; Zhang, P.; Li, X.; Zhu, J.; Li, H. X., Synchronical Pollutant Degradation and H2 Production on a Ti3+-Doped Tio2 Visible Photocatalyst with Dominant (001) Facets. *Appl Catal B-Environ* **2013**, *134*, 198-204.

98. Xu, J. W.; Jia, C. H.; Cao, B.; Zhang, W. F., Electrochemical Properties of Anatase Tio2 Nanotubes as an Anode Material for Lithium-Ion Batteries. *Electrochim Acta* **2007**, *52*, 8044-8047.

99. Zhu, K.; Wang, Q.; Kim, J. H.; Pesaran, A. A.; Frank, A. J., Pseudocapacitive Lithium-Ion Storage in Oriented Anatase Tio2 Nanotube Arrays. *J Phys Chem C* **2012**, *116*, 11895-11899.

100. Fang, H. T.; Liu, M.; Wang, D. W.; Sun, T.; Guan, D. S.; Li, F.; Zhou, J. G.; Sham, T. K.; Cheng, H. M., Comparison of the Rate Capability of Nanostructured Amorphous and Anatase Tio2 for Lithium Insertion Using Anodic Tio2 Nanotube Arrays. *Nanotechnology* **2009**, *20*.

101. Han, H.; Song, T.; Lee, E. K.; Devadoss, A.; Jeon, Y.; Ha, J.; Chung, Y. C.; Choi, Y. M.; Jung, Y. G.; Paik, U., Dominant Factors Governing the Rate Capability of a Tio2 Nanotube Anode for High Power Lithium Ion Batteries. *Acs Nano* **2012**, *6*, 8308-8315.

102. Lafont, U.; Carta, D.; Mountjoy, G.; Chadwick, A. V.; Kelder, E. M., In Situ Structural Changes Upon Electrochemical Lithium Insertion in Nanosized Anatalse Tio2. *J Phys Chem C* **2010**, *114*, 1372-1378.

103. Bresser, D.; Paillard, E.; Binetti, E.; Krueger, S.; Striccoli, M.; Winter, M.; Passerini, S., Percolating Networks of Tio2 Nanorods and Carbon for High Power Lithium Insertion Electrodes. *J Power Sources* **2012**, *206*, 301-309.

104. Moretti, A.; Kim, G. T.; Bresser, D.; Renger, K.; Paillard, E.; Marassi, R.; Winter, M.; Passerini, S., Investigation of Different Binding Agents for Nanocrystalline Anatase Tio2 Anodes and Its Application in a Novel, Green Lithium-Ion Battery. *J Power Sources* **2013**, *221*, 419-426.

105. Duan, J. X.; Hou, H. Y.; Liu, X. X.; Yan, C. X.; Liu, S.; Meng, R. J.; Hao, Z. L.; Yao, Y.; Liao, Q. S., In Situ Ti3+-Doped Tio2 Nanotubes Anode for Lithium Ion Battery. *J Porous Mat* **2016**, *23*, 837-843.

106.   Auer, A.; Portenkirchner, E.; Gotsch, T.; Valero-Vidal, C.; Penner, S.; Kunze-Liebhauser, J., Preferentially Oriented Tio2 Nanotubes as Anode Material for Li-Ion Batteries: Insight into Li-Ion Storage and Lithiation Kinetics. *Acs Appl Mater Inter* **2017**, *9*, 36828-36836.

107.   Bratic, M.; Jugovic, D.; Mitric, M.; Cvjeticanin, N., Insertion of Lithium Ion in Anatase Tio2 Nanotube Arrays of Different Morphology. *J Alloy Compd* **2017**, *712*, 90-96.

APPENDIX A

Supplementary Information

Table A.1   Raman peak shift and standard deviation (SD) of annealed TiO$_2$ nanotubes in different atmospheres with respect to O$_2$ control case. Green-colored cells indicate significant peak broadening

Peak Shift (cm^{-1})	Ar	N$_2$	WV
E$_g$(1)	-0.399	1.77	0.334
E$_g$(1) SD	0.246	0.233	0.225
E$_g$(2)	-0.761	0.732	-0.162
E$_g$(2) SD	0.737	0.350	0.364
B$_{1g}$(1)	-0.812	-0.062	0.0401
B$_{1g}$(1) SD	0.275	0.255	0.155
B$_{1g}$(2)+A$_{1g}$	0.0451	0.176	0.221
B$_{1g}$(2)+A$_{1g}$ SD	0.266	0.245	0.246
E$_g$(3)	-0.0617	-0.920	0.214
E$_g$(3) SD	0.157	0.163	0.403

Table A.2   Raman peak broadening and standard deviation (SD) of annealed TiO$_2$ nanotubes in different atmospheres with respect to O$_2$ control case. Green-colored cells indicate significant peak broadening

Peak Broadening (cm^{-1})	Ar	N$_2$	WV
E$_g$(1)	-0.291	1.32	0.188
E$_g$(1) SD	0.185	0.282	0.325
E$_g$(2)	2.74	17.6	-0.326
E$_g$(2) SD	4.60	16.4	3.43
B$_{1g}$(1)	-1.67	2.21	-1.74
B$_{1g}$(1) SD	1.18	1.14	1.16
B$_{1g}$(2)+A$_{1g}$	-0.877	1.67	0.545
B$_{1g}$(2)+A$_{1g}$ SD	1.56	0.786	0.565
E$_g$(3)	0.335	3.12	0.849
E$_g$(3) SD	1.75	1.63	1.59

Table A.3   Slope and strain values obtained from the Williamson-Hall plots of TiO$_2$ nanotubes annealed in different atmospheres. Crystallite size values calculated using Scherrer equation
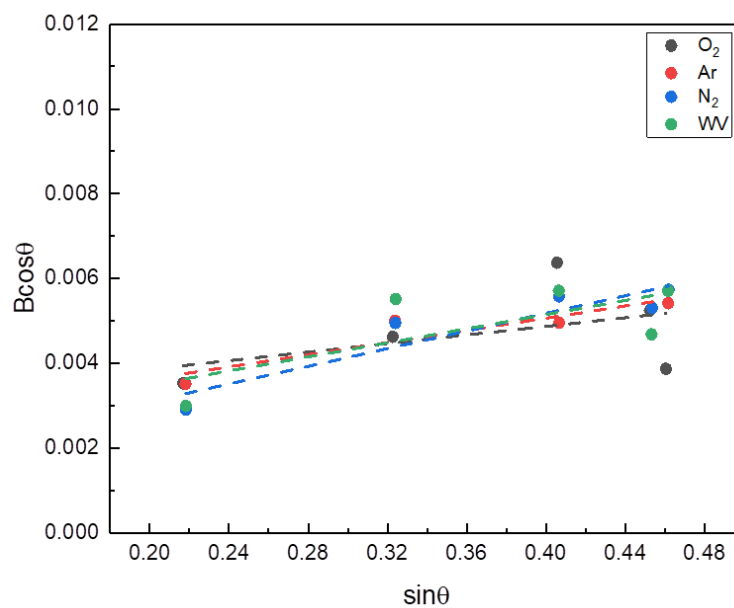
| Atmosphere	O$_2$	Ar	N$_2$	WV
Slope	0.00506	0.00718	0.01041	0.00831
Strain (%)	0.001265	0.001795	0.0026025	0.0020775
Crystallite Size (nm)	39	39	48	46
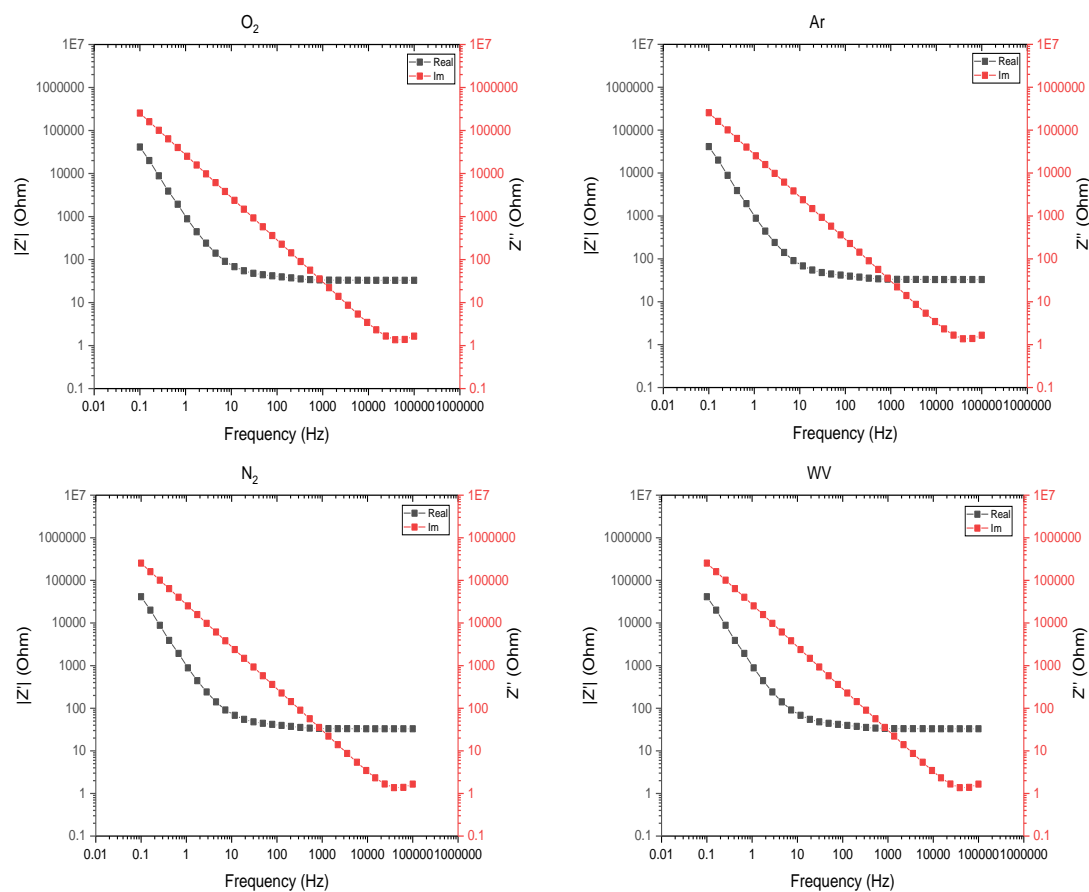
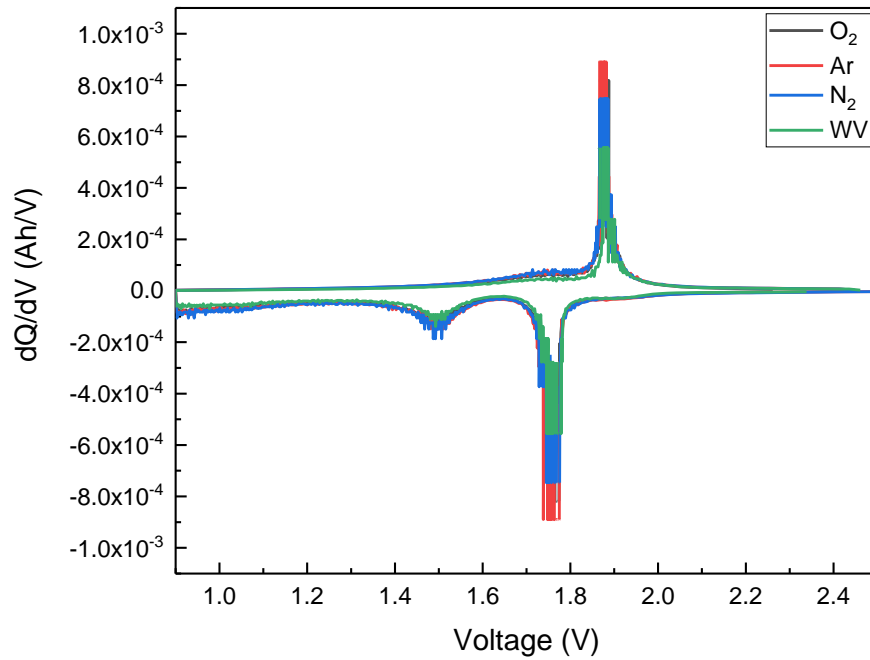**Figure A.1   Bode plots of anatase TiO$_2$ nanotubes annealed under various atmospheres**
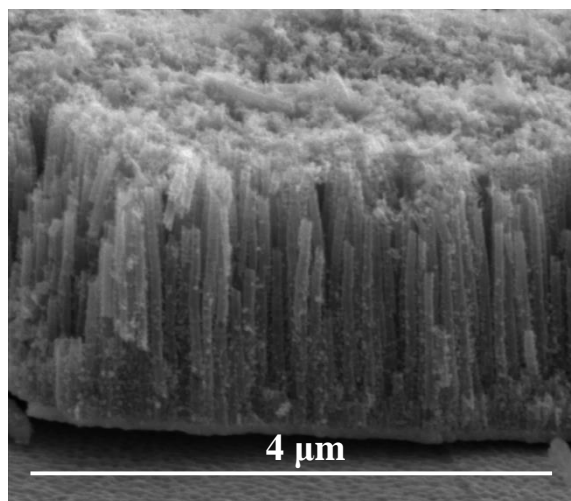
Figure A.2 Cross-sectional SEM image of anatase TiO₂ nanotubes annealed in WV atmosphere

Figure A.3 Williamson-Hall plots of anatase TiO₂ nanotubes annealed in different atmospheres
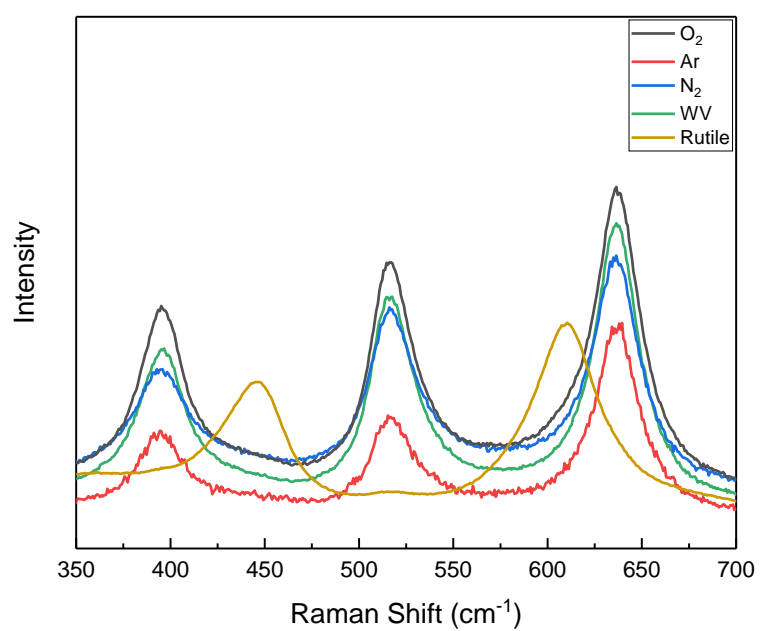
Figure A.4   Normalized Raman spectra of anatase TiO$_2$ nanotubes annealed in different atmospheres with rutile spectrum for comparison from 350-700 cm^{-1}

Figure A.5   1st cycle dQ/dV plots of anatase TiO$_2$ nanotubes annealed under different atmospheres